Science Advances

AAAS

advances.sciencemag.org/cgi/content/full/1/11/e1500421/DC1

Supplementary Materials for

A single-ligand ultra-microporous MOF for precombustion CO_2 capture and hydrogen purification

Shyamapada Nandi, Phil De Luna, Thomas D. Daff, Jens Rother, Ming Liu, William Buchanan, Ayman I. Hawari, Tom K. Woo, Ramanathan Vaidhyanathan

Published 18 December 2015, *Sci. Adv.* **1**, e1500421 (2015)
DOI: 10.1126/sciadv.1500421

The PDF file includes:

1. Materials and methods

All the organic chemicals were purchased from sigma aldrich. The nickel salts were procured from Alfa Aesar. Compounds and solvents were all used without any further purification.

Milligram scale synthesis of $Ni_9(\mu\text{-}H_2O)_4(H_2O)_2(C_6NH_4O_2)_{18}(H_2O)_{17}(CH_3OH)_4(C_4H_8O)_4$ (Ni-4PyC, 1):

A solvothermal reaction between Nickel carbonate(0.119g; 1mmol) and Pyridine-4-carboxylic acid (0.244g; 2mmol) in a solution containing1.5ml THF+2.5mlwater +2ml MeOH was carried out at 150^{o}C for 72hrs. A bright blue colored polycrystalline product was isolated by filtration and was washed with plenty of water and methanol. The air dried sample gave a yield of ~75% (based on Ni). The PXRD pattern indicated this to be a pure phase of **1**. We have also prepared 10-25gms of this sample with an easy scale-up procedure. CHN analysis (calculated values within brackets: C: 43.45 (43.2210); H: 3.62 (4.7039); N: 7.02 (7.0880)%. It was noted that the presence of THF was critical to the formation of this phase. However, it could be exchanged in a post synthetic manner for methanol. Also, the use of nickel nitrate and other salts of nickel could not result in a pure phase of **1**.

10gm synthesis:

About 2.975g of Nickel carbonate anhydrous was added to 6.1g of 4-PyC in a solution containing 25ml water + 20ml MeOH + 10ml THF, contents were stirred for 2 hours at room temperature. Contents were placed in a 123mL teflon lined Parr stainless steel autoclave and heated at 150^{o}C for 72hrs. A bright blue colored polycrystalline product identical in appearance to the smaller scale preparation was obtained. The air dried sample gave a yield of ~90% (based on Ni). The PXRD, TGA and N_2 & CO_2 gas uptakes matched well with the small scale sample.

2. Single crystal structure determination:

Single-crystal data was collected on a Bruker SMART APEX four-circle diffractometer equipped with a CMOS photon 100 detector (Bruker Systems Inc.) and with a Cu Kα radiation (1.5418 Å). The incident X-ray beam was focused and monochromated using Microfocus (IμS). Crystal of **1** was mounted on nylon Cryo loops with Paratone-N oil. Data was collected at 173(2) K. Data was integrated using Bruker SAINT software and was corrected for absorption using SADABS. Structure was solved by Intrinsic Phasing module of the Direct methods and refined

using the SHELXTL 97 software suite. All non-hydrogen atoms were located from iterative examination of difference F-maps following which the structure was refined using least-squares method. Hydrogen atoms were placed geometrically and placed in a riding model. Some of the 4-PyC units in the structure of **1** were disordered over two sites and have been modeled satisfactorily using SIMU and DELU commands.

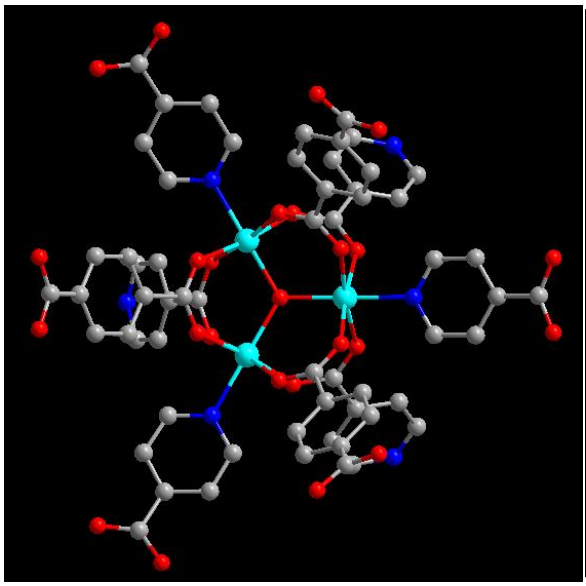

Left: Shown is the trimeric Nickel hydroxo pyridine carboxylate-terephthalate cluster with a D_3h symmetry present in the compound reported by X.M.Chen and co-workers.(*Ref.45 of the main text*) These are generated in Dimethyacetamide medium.

Bottom: The two different dimeric Nickel(μ_2-H_2O) pyridine carboxylate clusters present in **1**. These are lower in symmetry. And are generated in an aqueous medium (H_2O+CH_3OH+THF, pH=4.0).

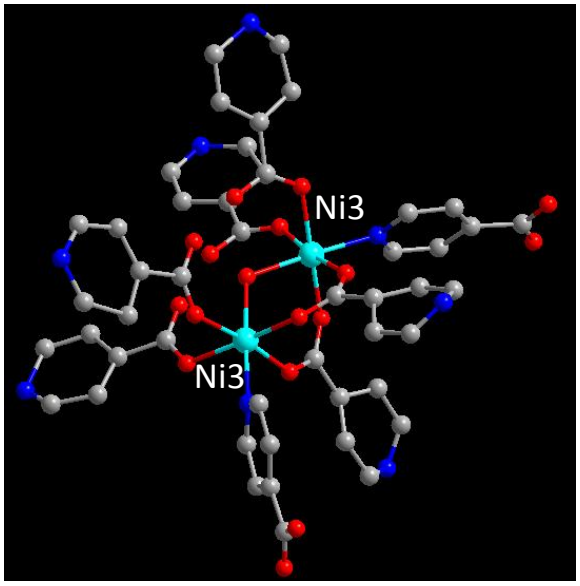

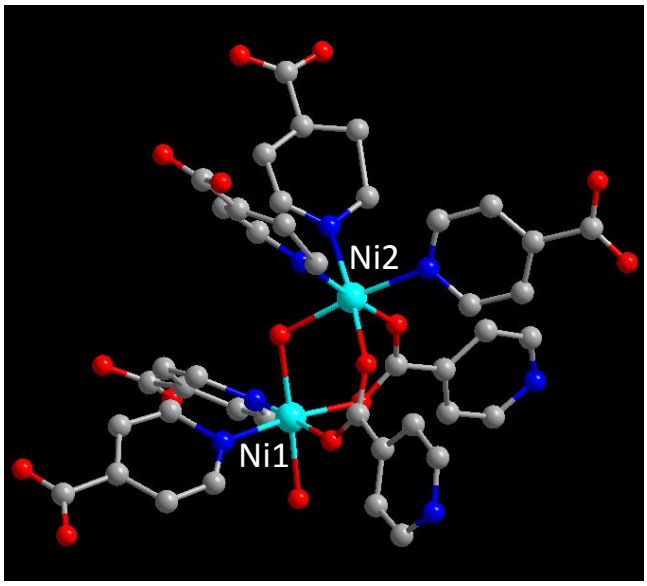

Figure S1. Comparison of the Nickel clusters present in **1**, with the recently reported nickel clusters in a pyridine carboxylate based MOF. Note that these hydroxo and water based clusters have much better stability toward hydrolysis in air as compared to the oxo-type clusters present in many widely studied MOFs synthesized in DMF or DMA medium. These molecular level features could play a critical role in the hydrolytic stability of the material. The dimers formed of Ni3 atoms connects to the other dimers (Ni1,Ni2) and also to the isolated nickel octahedra formed by Ni4, not shown here.

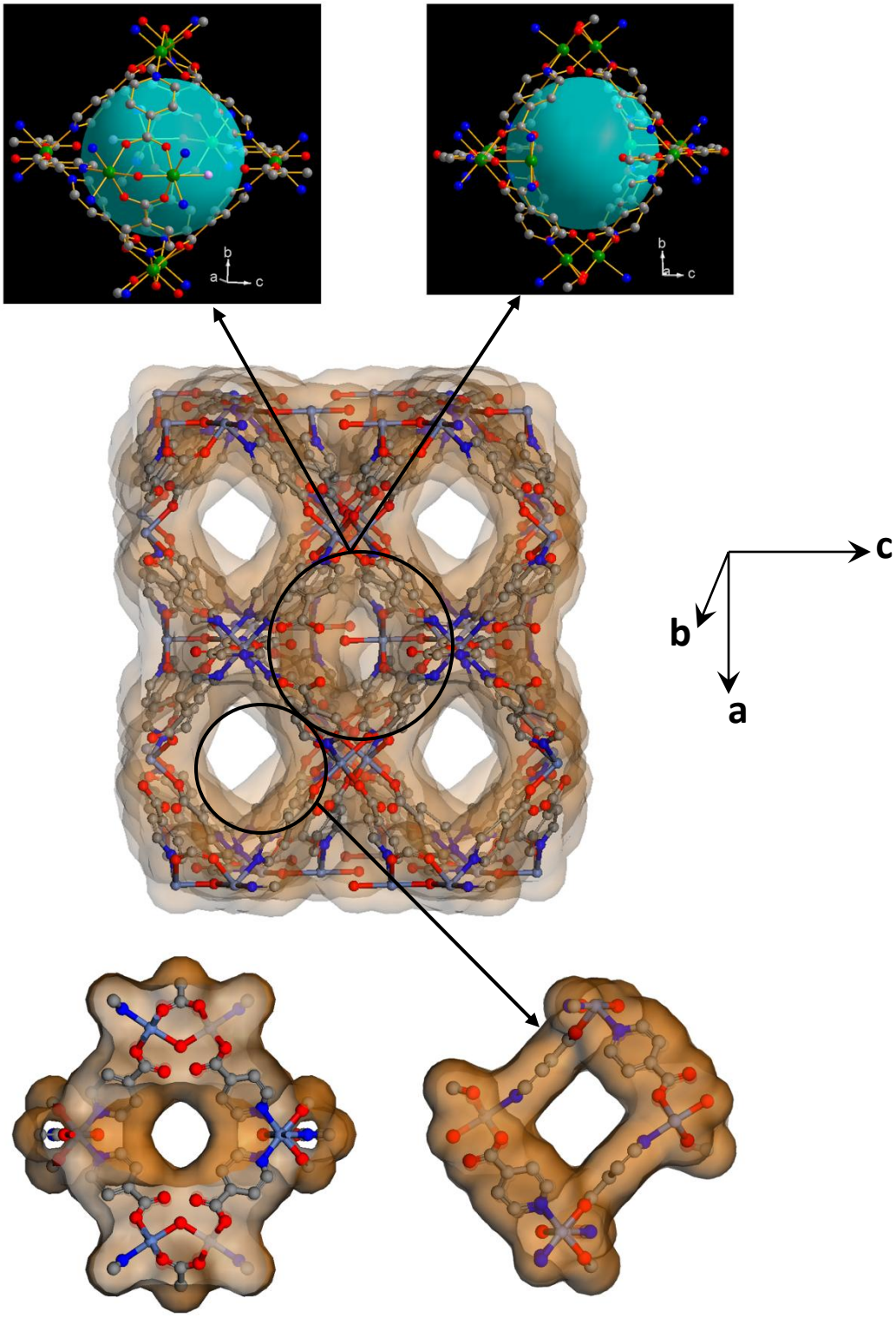

Figure S2. Top: The water lined cavities in **1**, these are not accessible even upon the removal of cooridnated water (Top right) and do not contribute to overall porosity. Shown are the two accessible channels in **1**, the circular one is along the c-axis, while the square shaped one is along the b-axis. Notice that the former is polar.

Table S1. CO_2 uptakes at 195K and 273K for selected ultra- and microporous MOFs.

MOF	**Pore dia. (Å)**	**CO_2 uptake (mmol/g)**		**HOA (KJ/mol)**	**Reference**
		195K	***273K***		
BioMOF-11	5.80(cavity) & 5.20x5.20 (window)[a]	------	6.56	33.1	*Chem. Sci.* **4**, 1746 (2013)
BioMOF-12	5.70(cavity) & 5.20x5.00 (window)[a]	------	4.5	38.4	*Chem. Sci.* **4**, 1746 (2013)
ZIF-78	7.10[e]	------	3.34	------	*J Am Chem Soc.* **131**, 3875 (2009)
ZIF-69	7.80[e]	------	3.03	------	*J Am Chem Soc.* **131**, 3875 (2009)
Cu-TDPAT	cub-O_h size-12[a] T-T_d size-9.1[a] T-O_h size-17.2[a]	------	10.1	42.2	*Angew. Chem. Int. Ed.* **51**, 1412 (2012)
SNU-M10	4.85 x 12.12 and 1.21x4.37[a]	5.4	3.2	------	*Angew. Chem. Int. Ed.* **48**, 6865 (2009)
SNU-M11	1.16 x 6.29[a]	5.35	Very low		*Angew. Chem. Int. Ed.*, **48**, 6865 (2009)
Cu-BTTri	----------	19	3.9	22	*J. Am. Chem. Soc.* **131**, 8784 (2009)
Ni(4-PyC)	**3.48, 4.80[b]**	**10.8**	**5.53**	**34**	**Present work**
Mg(DOBDC)	10.81[b]	------	10.30	48	*J. Am. Chem. Soc.* **130**, 10870 (2008)
IR MOF-11	9.03[b]	------	------	------	*Energy Environ.Sci.* **3**,268 (2010)
IR MOF-12	13.02[b]	------	------	------	*Energy Environ.Sci.* **3**, 268 (2010)
IR MOF-13	10.00 [b]	------	------	------	*Energy Environ.Sci.* **3**, 268 (2010)
IR MOF-14	13.80[b]	------	------	------	*Energy Environ.Sci.* ***3,*** 268, (2010)
PCN-61	12.00[b]	------	5.71	21.4	*J.Am.Chem.Soc.* **133**,748 (2011)
NJU_Bai7	---------	------	2.95	40.5	*J. Am. Chem. Soc.* **135**, 562 (2013)
SYSU	6.3 × 6.3[a]	------	4.5	28.2	*J. Am. Chem. Soc.*

					135, 562 (2013)
$[Ni_3(\mu_3OH)(ina)_3(bdc)_{1.5}]\cdot 2.5DMA\cdot CH_3OH$	7.80[a] 7.40[a] 5.20[a]	9.35	------	------	*Nature Comm.**3***, 1 (2011)
ZTF-1	4.50[**a**]	------	5.35	**22.5**	*Chem. Commun.* **47**, 2011 (2011)
ZnAtzOx	4.7 & 5.15[b]	4.30	4.25	40	*Science*, **650**, 330 (2010)
ZnAtzPO4	5.6 & 7.8[b]	4.85	3.2	32	*Angew. Chem. Int. Ed.* **51**, 1826 (2012)
BioMOF-1	12.77x12.77[a] 9.97x9.97	------	3.41	21.9	*J. Am. Chem. Soc.* **132**, 5578 (2010)
TMA@BioMOF-1	,,	------	4.46	23.9	*J. Am. Chem. Soc.* **132**, 5578 (2010)
TEA@BioMOF-1	,,	------	4.16	26.5	*J. Am. Chem. Soc.* **132**, 5578 (2010)
TBA@BioMOF-1	,,	------	3.44	31.2	*J. Am. Chem. Soc.* **132**, 5578 (2010)
SIFSIX-3-Cu	3.50[e]	------	2.54(298K)	54	*DOI: 10.1038/ncomms.* 5228 (2014)
SIFSIX-3-Zn	3.84[e]	------	2.40(298K)	45	*DOI: 10.1038/ ncomms.* 5228 (2014)

[a]Experimentally determined.
[b]Calculated from Single crystal structure (do not factor in the Van Der waal radii).
------- = Data not available.

3. Analytical characterizations

Powder X-ray diffraction:

Powder XRDs were carried out using a Rigaku Miniflex-600 instrument and processed using PDXL software.

Thermogravimetric Analysis:

Thermogravimetry was carried out on NETSZCH TGA-DSC system. The routine TGAs were done under N_2 gas flow (20ml/min) (purge + protective) and samples were heated from RT to 550^{o}C at 2K/min.

For the cycling experiments, no protective gas was used, and the gas flows were systematically switched between CO_2 and N_2 on the purge lines. The methanol exchanged sample of **1** was loaded on to the Pt pans and evacuated for 16hrs prior to the runs. TGA and DSC calibration and corrections runs were done just prior to carrying out the cycling experiments. This seemed to be critical to obtain accurate data from these cycling experiments. Without these systematic preparations, the data were found to be highly over estimated.

IR spectroscopy:

IR spectra were obtained using a Nicolet ID5 attenuated total reflectance IR spectrometer operating at ambient temperature. The KBr pellets were used.

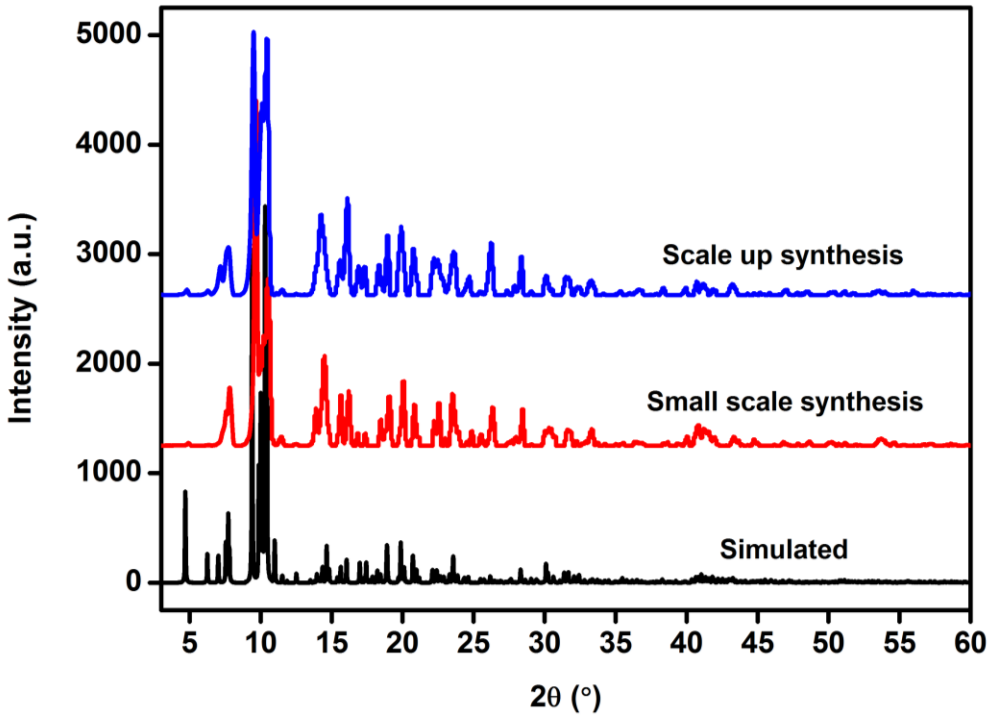

Figure S3. Comparison of the powder X-ray diffraction patterns of **1** with the ones simulated from single crystal data.

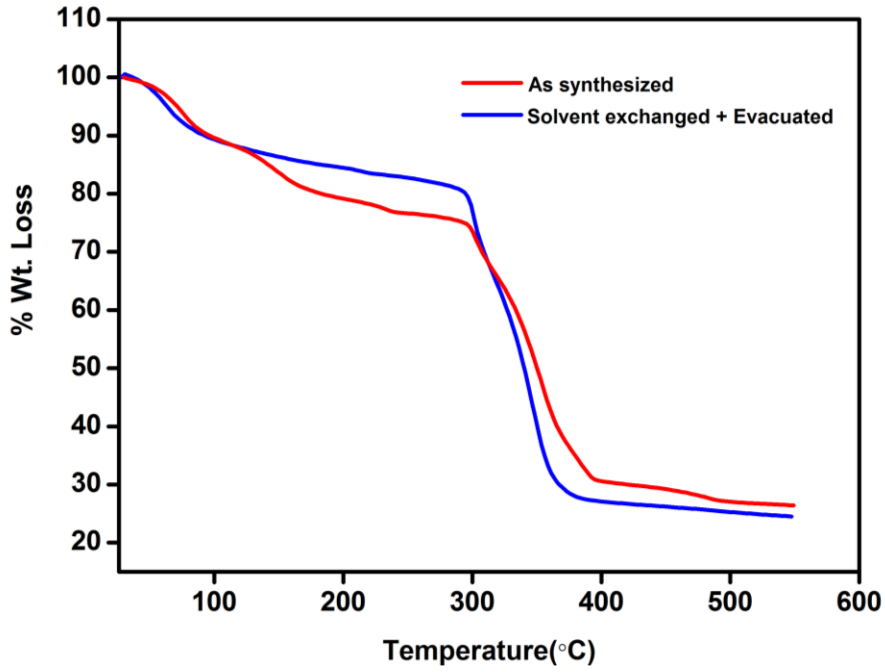

Figure S4. TGA plots of the as-made sample and the completely activated sample.

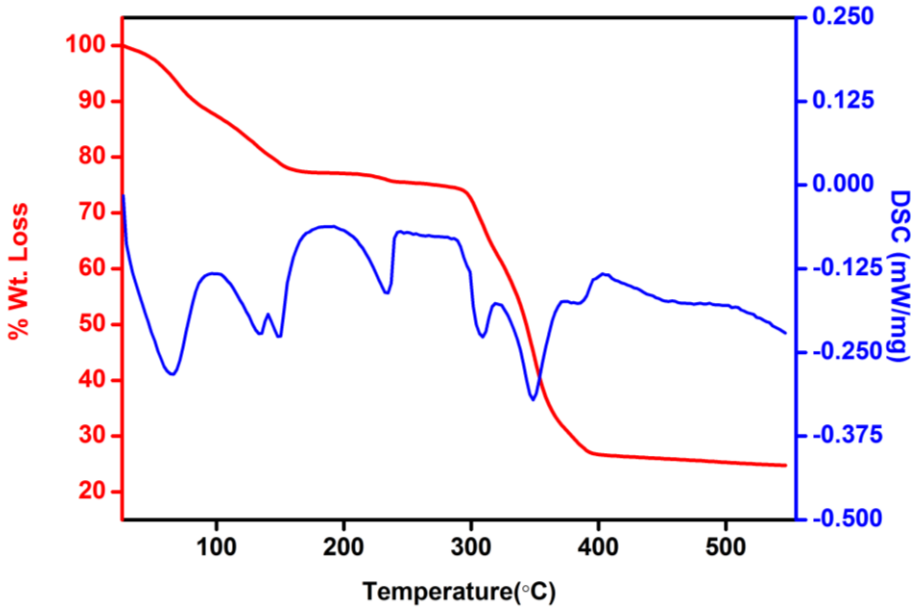

Figure S5. TGA carried out on the methanol exchanged sample of **1**. The weight loss have been calculated using the formula $Ni_9(\mu\text{-}H_2O)_4(H_2O)_2(C_6NH_4O_2)_{18}(H_2O)_{17}(CH_3OH)_4(C_4H_8O)_4$ (M. Wt. **3557.2**) . All the volatile solvent molecules are removed by 100^{o}C (4 THF + 4 MeOH + 2 H_2O(surface adsorbed) loss, calc:12.71%, obsd: 12.7), while most of the free solvent water and the coordinated water come off at 180^{o}C (calc: 9.61%; obsd: 10.21). Some of the water molecules (2.02%) do not leave the structure even at 200^{o}C. It is highly likely that this is some of the bridging water molecules (calc: 2.05%) that are crucial for holding the framework together. The loss of this 2% water triggers the collapse of the structure.

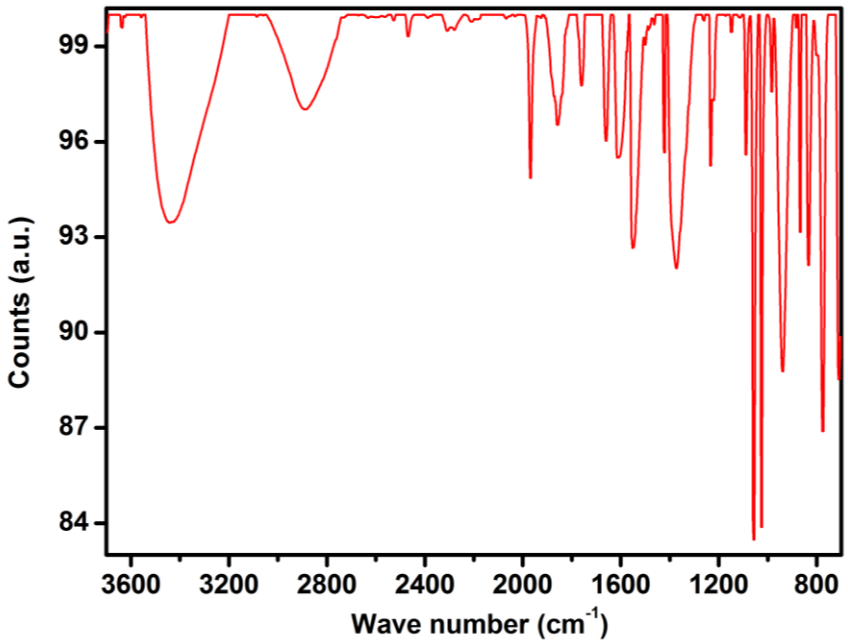

Figure S6. Infra red spectra of **1**, showing the various stretching and bending modes present . Selected peaks: IR (KBr pellet, cm-1): ν(O-H)solvent: 3460s; ν(C-H): 2989; ν(COO): 1656s and 1594νs, ν(COO)s 1423s, 1373 νs; ν (C=C): 1200 to 800. (*Source: Infrared and Raman Spectra of Inorganic and Coordination Compounds, Part B, Applications in Coordination, Organometallic, and Bioinorganic Chemistry, 6th Edition, Kazuo Nakamoto*)

4. Adsorption Analysis

All gas sorption isotherms were measured on a Micromeritics ASAP 2020HD or 3-FLEX instrument using ultra-high purity gases (≥4.8 grade). Samples were transferred to a glass tube for analysis, with dual stage activation: The as-made samples were solvent exchanged by soaking 200mg in 7ml methanol (reagent grade) for 72 hours, with the solvent being replenished every 24hrs. Following this the 100mg of the solvent exchanged sample was transferred to analysis glass vial and evacuated at 70°C on the degas port for 36hrs (10^{-6} mbar), at which point the outgas rate was ≤ 2 μbar/min.

The rate of adsorption experiments were carried out on the Micromeritics ASAP2020HD instrument equipped with a ROA software capabilities. Numerous equilibrium points and associated kinetic data were recorded at 273K, however for data analysis regularly spaced 11 CO_2 loading points were picked out in the interval of 0 to 1000mbar.

Langmuir Fits:

In most cases the isotherms were fit to the Single-Site Langmuir (SSL) equation. Modified Langmuir equations were utilized to account for significant errors in the Langmuir model. It is widely known that even small fitting errors will have a devastating impact on selectivity calculations. Note: 195K CO_2 and N_2 isotherms were not used as the temperature is too close to the CO2 phase change temperature.

The isotherms were fit by solving the Langmuir equation using the solver function in Microsoft Excel following a similar protocol to Keller *et al* (*Nat. Protoc.* **2010**, *5*, 267–81). Utilizing this routine circumvents some of the problems associated with favoring either high or low pressure regions when linearizing the Langmuir equation (Richter et al. *Chem. Eng. Sci.* **1989**, *44*, 1609) and offers a balanced approach.

Single-Site Langmuir (SSL):

$$q_i = q_m \frac{K_i P}{1 + K_i P}$$

Dual-Site Langmuir (DSL):

$$q_i = q_{m,1} \frac{K_1 P}{1 + K_1 P} + q_{m,2} \frac{K_2 P}{1 + K_2 P}$$

Dual-Site Langmuir (DSL):

$$q_i = q_{m,1} \frac{K_1 P}{1 + K_1 P} + q_{m,2} \frac{K_2 P}{1 + K_2 P}$$

Ideal Adsorbed Solution Theory (*IAST*):

IAST calculations were undertaken as described by Prausnitz *et al* (*AIChE J.* **1965**, *11*, 121). The selectivity equation is provided below.

Selectivity:

$$S_{1,2} = \frac{q_1 / q_2}{P_1 / P_2}$$

Table S2. CO_2 adsorption and desorption data of **1** at 195K

Absolute Pressure (mmHg)	Amount adsorbed (mmol/g)
0.326985	0.994017
0.995764	1.802344
1.664418	2.463762
2.810029	3.395624
4.665151	4.677797
9.078659	6.326634
12.98214	6.955803
17.32202	7.374822
21.54473	7.647347
35.99794	8.201156
48.14801	8.476302
60.27357	8.679774
79.99664	8.918617
90.18822	9.016615
100.3322	9.1075
129.4362	9.302295
143.3174	9.383777
157.9865	9.462093
171.7103	9.526138
186.3498	9.589897
201.0119	9.649938
214.5985	9.699312
229.3281	9.752921
243.5784	9.799399
272.3251	9.880699
300.1215	9.957195
328.6635	10.02957
344.4715	10.07298
357.3972	10.1043
385.7692	10.16378
414.7627	10.22106
443.475	10.27739
473.2558	10.33604
500.6811	10.38649
529.3032	10.43835
557.9955	10.49106
586.8552	10.54366
615.5965	10.59726
645.4814	10.64686
674.0063	10.69388
702.613	10.74472
666.5468	10.69284

635.6925	10.64847
604.3189	10.59939
574.3057	10.55156
542.7305	10.49995
512.0017	10.45088
482.4595	10.4034
450.4844	10.34625
419.851	10.28622
388.6154	10.21997
357.8197	10.15184
327.6313	10.08352
296.299	10.00777
265.7375	9.926239
235.2899	9.83405
204.7804	9.731097
173.999	9.609619
143.3287	9.457468
112.362	9.269522
81.5944	9.008897
50.62249	8.595077
35.36989	8.2579
19.97945	7.627915
12.14666	6.920757
4.473279	4.62628
1.00466	1.833463

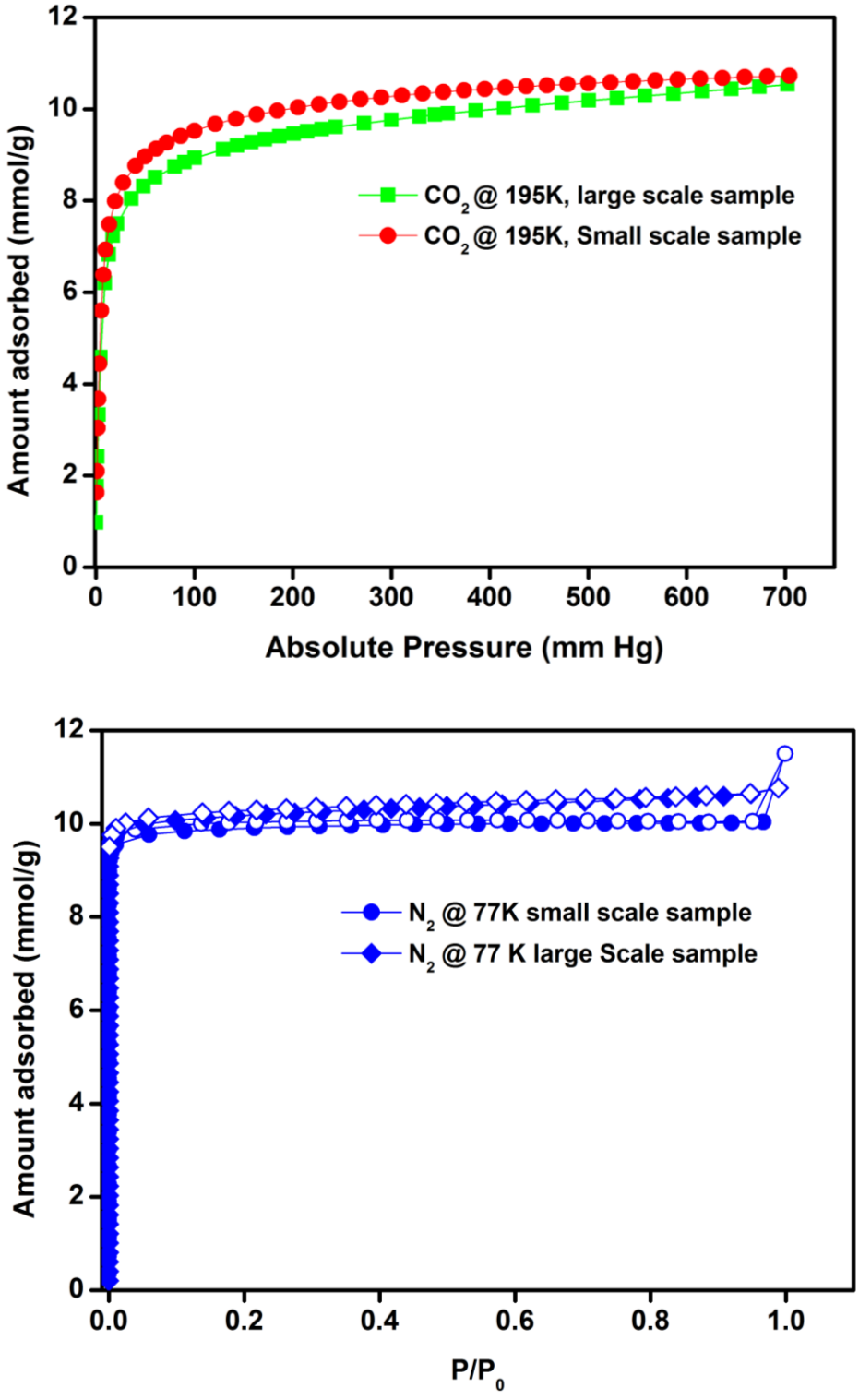

Figure S7. Comparison of the 195K CO_2 and 77K N_2 adsorption isotherms of the mg and gm scale syntheses, showing the laboratory scale scalability. The DFT done to the adsorption branch of the isotherm gives a pore size of 5.76Å and is consistent with the PSD obtained from the Howarth-Kawazoe.

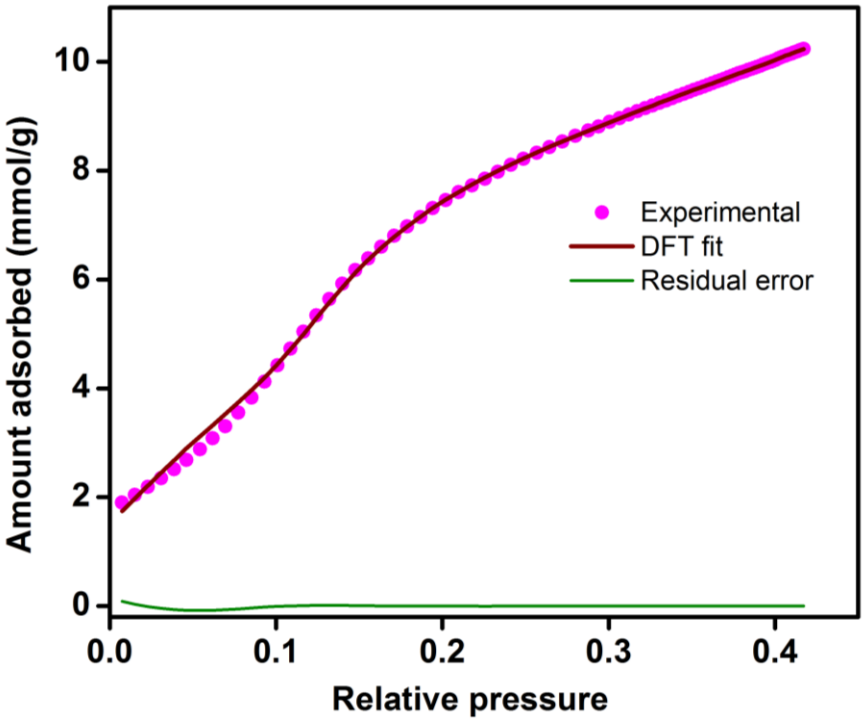

Figure S8. Shows the fitting comparison obtained for the NLDFT fit done to the adsorption branch of the 195K CO_2 data.

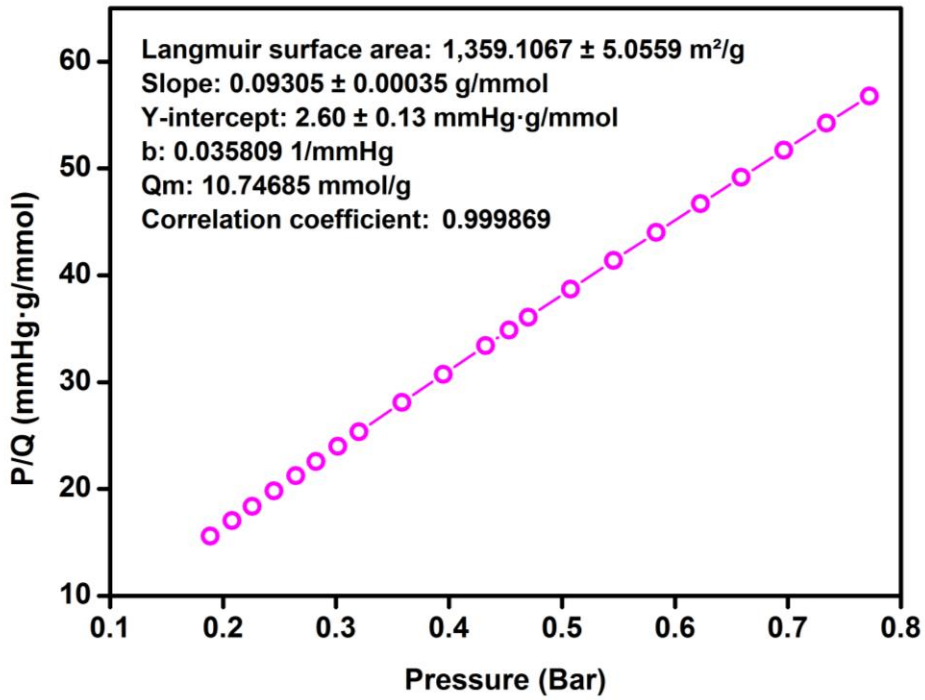

Figure S9. Shows the fitting comparison obtained for the Langmuir model done to the adsorption branch of the 195K CO_2 data.

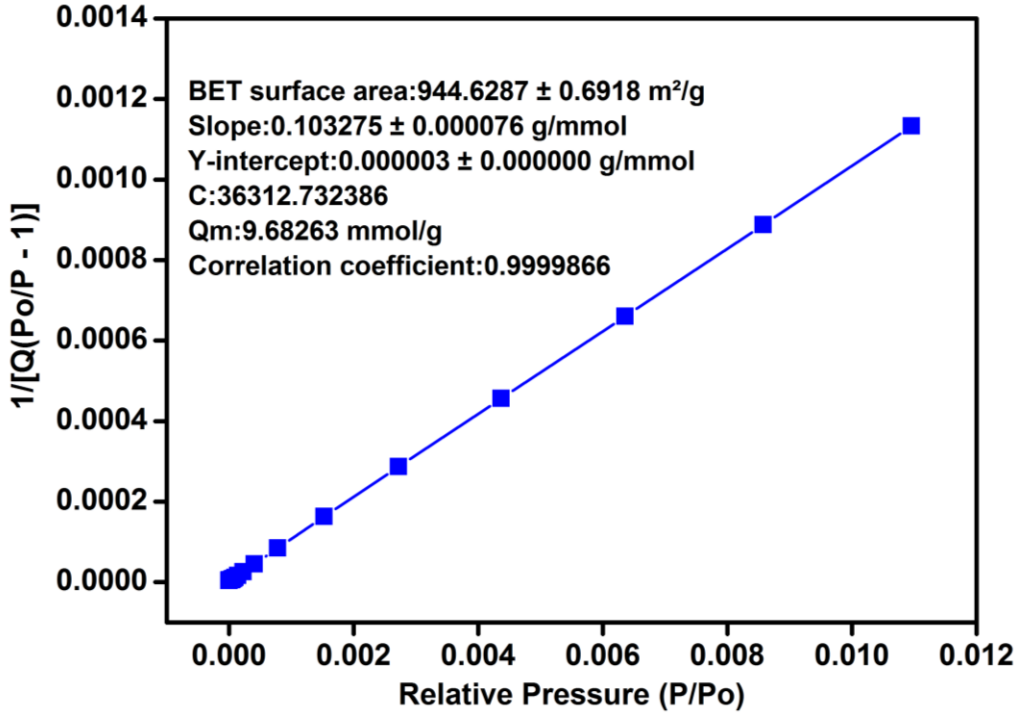

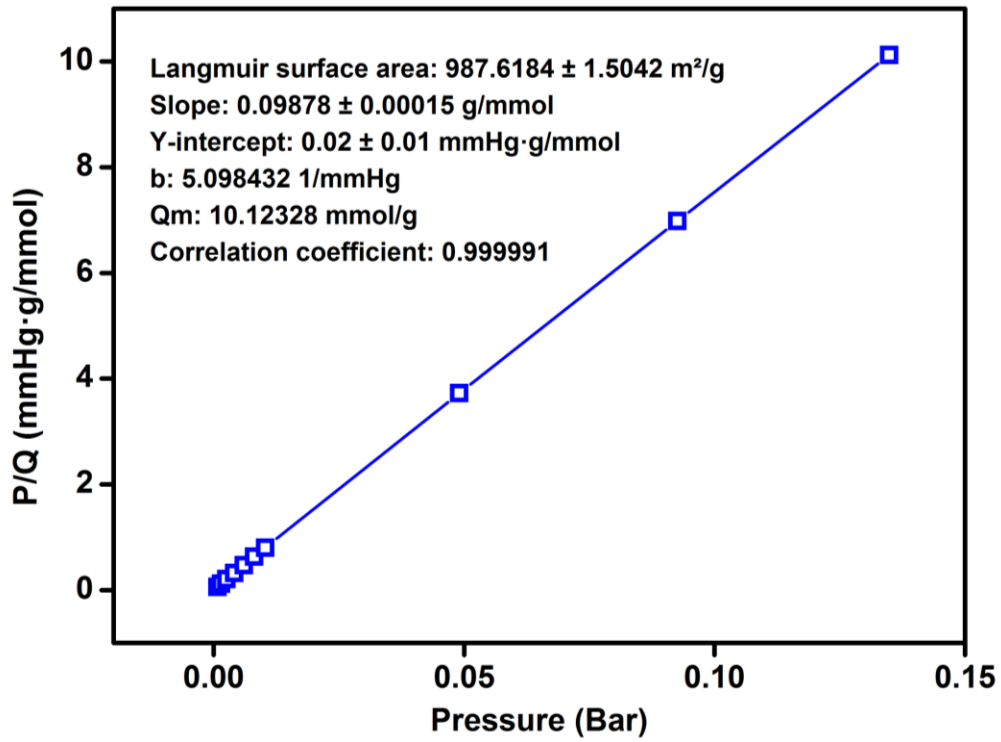

Figure S10. BET and Langmuir fits from the 77K N_2 data.

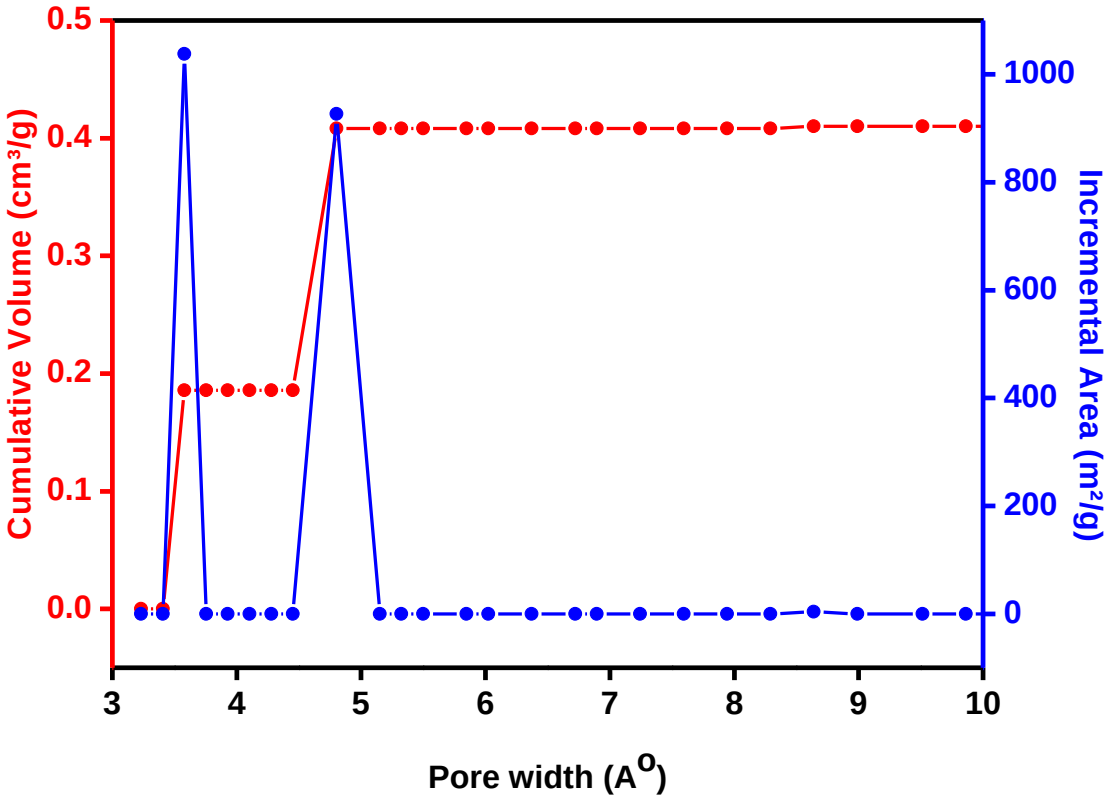

Figure S11. Pore size distribution in **1** obtained by fitting the NLDFT model to the 195K CO_2 adsorption branch . Note the presence of a bimodal distribution with pores of dimensions ~3.5 and ~4.8 Å. This agrees well with the ultra-micropores observed in the single crystal structure.

Column Breakthrough Test Set-up, Procedure:

About 10-12 gm of **1** was loaded onto a stainless column fitted with mass flow controllers and pressure gauges to control the inlet and outlet pressures. **1** was subjected to a pretreatment by heating at 70^{o}C under vacuum for 24 hours within the adsorption column. The CO_2/H_2 and CO_2/He breakthrough experiments were carried out using the RuboLab / Rubotherm VariPSA system. This instrument allows the measurement of breakthrough curves (BTC) on solid sorbent materials. Based on the sorbent the system settings were optimized. The adsorber column was designed to be approx. 8 ml in volume. To measure the sorption based temperature (adsorption front), three temperature sensors were integrated to measure the temperature at two different positions within the adsorber bed. (Thermocouple type K, 3 mm diameter of temperature sensor). The gas flow across the column was controlled using a micrometering valve. All measurements were performed by using a gas flow of 0.75 L/min. While the adsorption of CO_2 was indicated by its retention time on the column, the complete breakthrough of CO_2 was indicated by the downstream gas composition reaching that of the feed gas. Using the formula,

number of mole adsorbed $n = F * C_i * t$, where F = molar flow, C_i = concentration of i^{th} component and t = retention time, the CO_2 uptake was calculated to be 2.6mmol/g for the $40CO_2/60$He mixture and this uptake closely matched with the uptake obtained for the $40CO_2/60H_2$ mixture.

5. Pore size determination from Positron Annihilation Lifetime Spectroscopy (PALS)

Experiment

The PALS measurements were carried out at the positron facility of the NC State University. SN-322 or Ni-(4PyC), **1**, was characterized at RT before and after its thermal activation. Due to the small quantity of **1**, the aqueous ^{22}NaCl positron source was deposited and dried on a piece of Tungsten foil (4mm in diameter), and the sample was directly placed on top of this one-sided source. In this configuration, half of the positrons from the source would be emitted towards the Tungsten foil. However, with the help of the high atomic number of Tungsten, approximately 40% of these positrons would be backscattered into the sample. Therefore, there would be ~70% of all the positrons implanted into the sample, while 30% into the Tungsten. The source and the sample were under vacuum throughout the process of heating and PALS measurement. The first time annealing of the sample was conducted at 90°C for 24hrs. Another annealing at 100°C for 24hrs was done after the sample cooled down to RT and the PALS spectrum was taken.

PALS Results

The background subtracted and peak normalized PALS spectra of the as-received and the annealed sample are shown together in figure S12. There is a slight change in PALS spectrum after the annealing at 90°C, however, it is obvious that the most dramatic change occurs after the heating to 100°C. The spectra were best fitted, using a least-square fitting program, POSFIT, with three lifetime components, as shown in table S3. Here the third lifetime (τ3) and its intensity (I3) are due to the o-Ps annihilation that is most interesting to us. Based on the well-established Tao-Eldrup model (S. J. Tao, *J. Chem. Phys*. 56, 5499 (1972), M. Eldrup, *Chem. Phys.* 63, 51 (1981), this 1.2-1.4 ns component can be converted to a spherical pore size of 3.9-4.4Å, which is fairly consistent with the chemical structure of **1** as well as the CO_2 adsorption result at 195K. In the CO_2 adsorption data, however, the measured pore size distribution is bimodal, while the PALS results appear to be consistent with the average of the sizes of these two pore populations. This is not surprising since the two pore sizes measured by CO_2 adsorption, ~3.6Å and ~4.9Å, are very close to each other, corresponding to o-Ps lifetimes of 1.1ns and 1.6ns and could not have been separated from the fitting program.

Table S3. Discrete fitting results of Ni-4PyC, 1

Treatment	τ1 (ns)	I1 (%)	τ2 (ns)	I2 (%)	τ3 (ns)	I3† (%)
As Received	0.263±0.008*	72±2	0.620±0.031	24.8±1.7	1.44±0.07	3.54±0.64
90°C, 24 hrs	0.271±0.008	63±3	0.639±0.036	32.8±1.5	1.21±0.09	4.6±1.7
100°C, 24 hrs	0.228±0.011	51±3	0.494±0.019	34.6±2.6	1.24±0.01	14.1±0.4

*Errors are statistical errors of the fitting
†The o-Ps intensities are not corrected to account for the fact that 30% of the positrons are implanted into the Tungsten source
Note: SN322 refers to material Ni-4PyC, **1**.

The o-Ps intensity (I3 in table S3) increased noticeably after the first annealing at 90°C, and jumped drastically from 4.6% to 14.1% after heating to 100°C. Within the same chemical environment, this change of o-Ps intensity can be directly correlated to the change of porosity. Obviously, most of the activation of the SN-322 occurred after the second annealing when the porosity increased significantly.

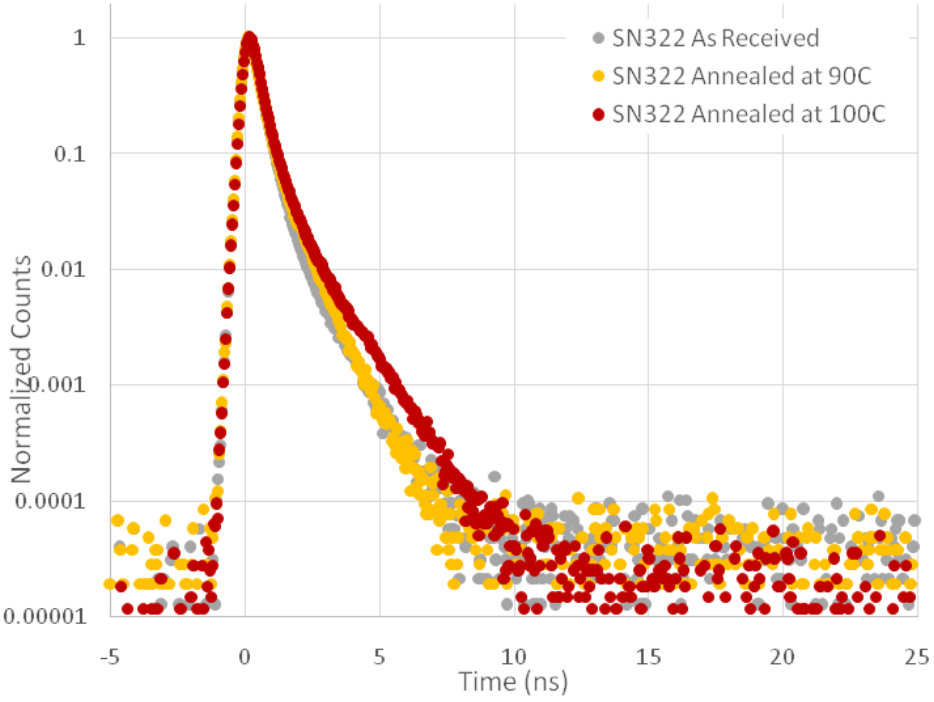

Figure S12. The background noise corrected and peak normalized PALS spectra of SN322 taken at RT before and after the thermal annealing. Note: SN322 refers to material Ni-4PyC, **1**.

6. VIRIAL:

The CO_2 adsorption data for **1** were measured from 0- 1bar at 263, 273, 283, 303K and were fitted by the virial equation (1) .

*ln(P) = ln(Va)+(A0+A1*Va +A2*Va^2 …+ A6*Va^6)/T+(B0+B1*Va)*..... (1)

Where P is pressure, Va is amount adsorbed, T is temperature, and A0, A1, A2 … , A4 and B0, B1

are temperature independent empirical parameters (Figs. S.15 and S16)

Table S4: Summary of the fitted Virial parameters

A0	-4015.961213
A1	769.7356334
A2	-169.8811741
A3	7.424735813
A4	0.247999083
B0	17.90621071
B1	-2.117488599
B2	0.52322824

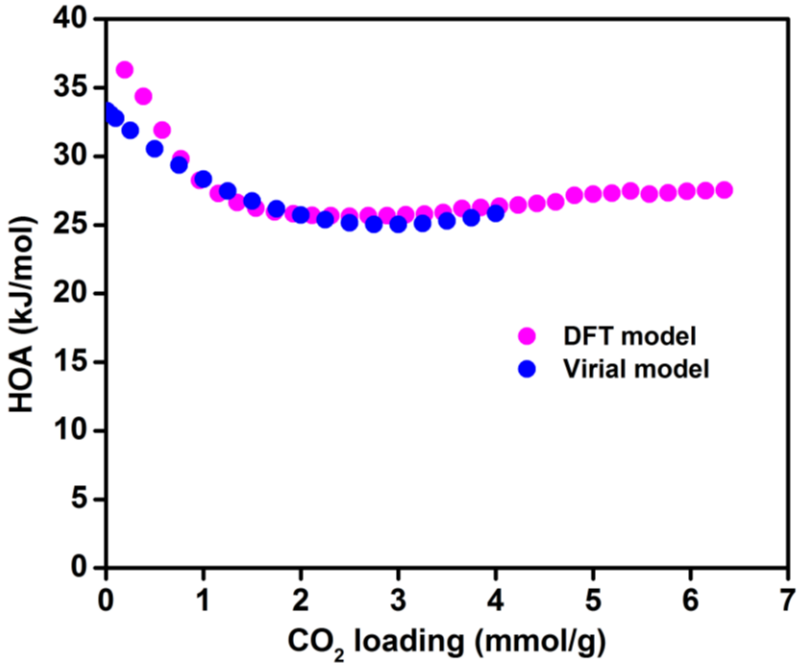

Figure S13. Comparison of the HOA trend obtained from the virial and DFT modeling done using the CO_2 isotherms carried out at -10°C, 0°C, +10°C and +30°C.

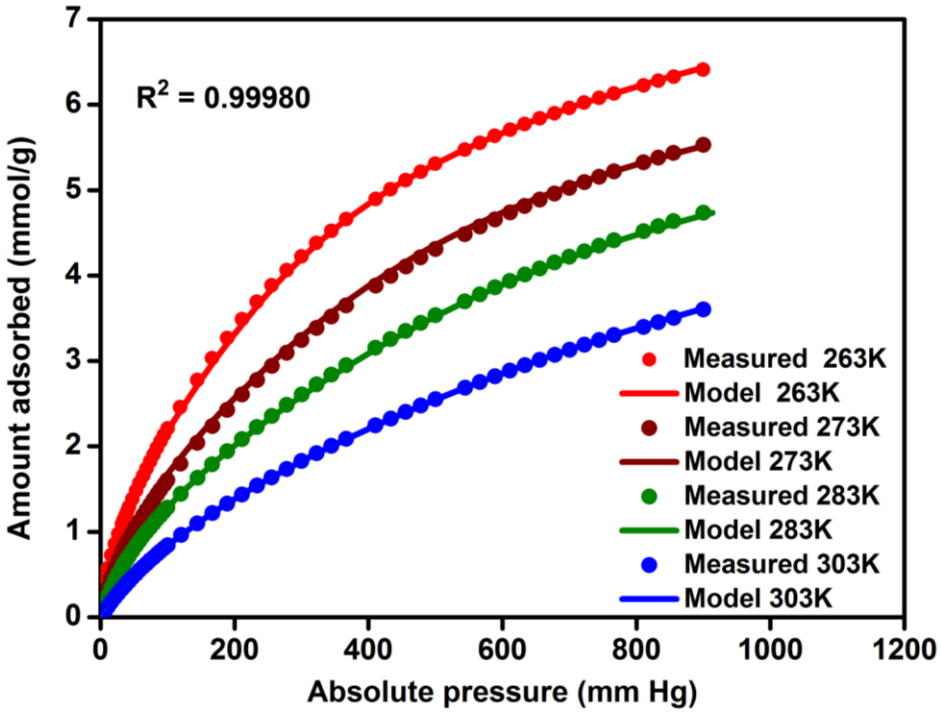

Figure S14. Comparison of experimental isotherms to the ones obtained from virial modeling carried out using CO_2 isotherms collected at -10°C, 0°C, +10°C and +30°C.

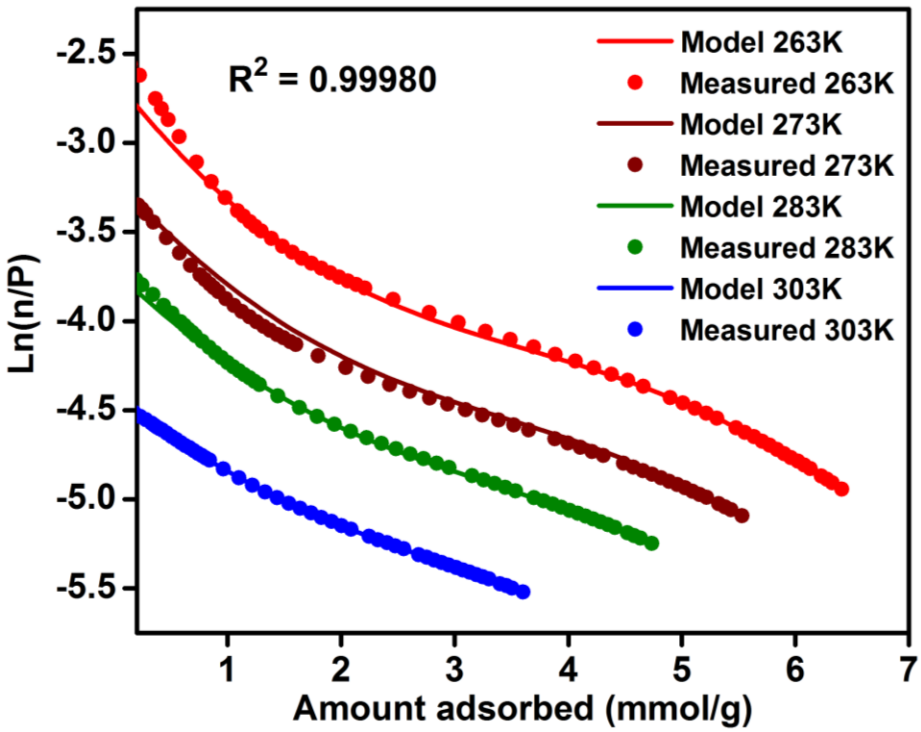

Figure S15. Virial plots carried out using CO_2 isotherms collected at -10°C, 0°C, +10°C and +30°C.

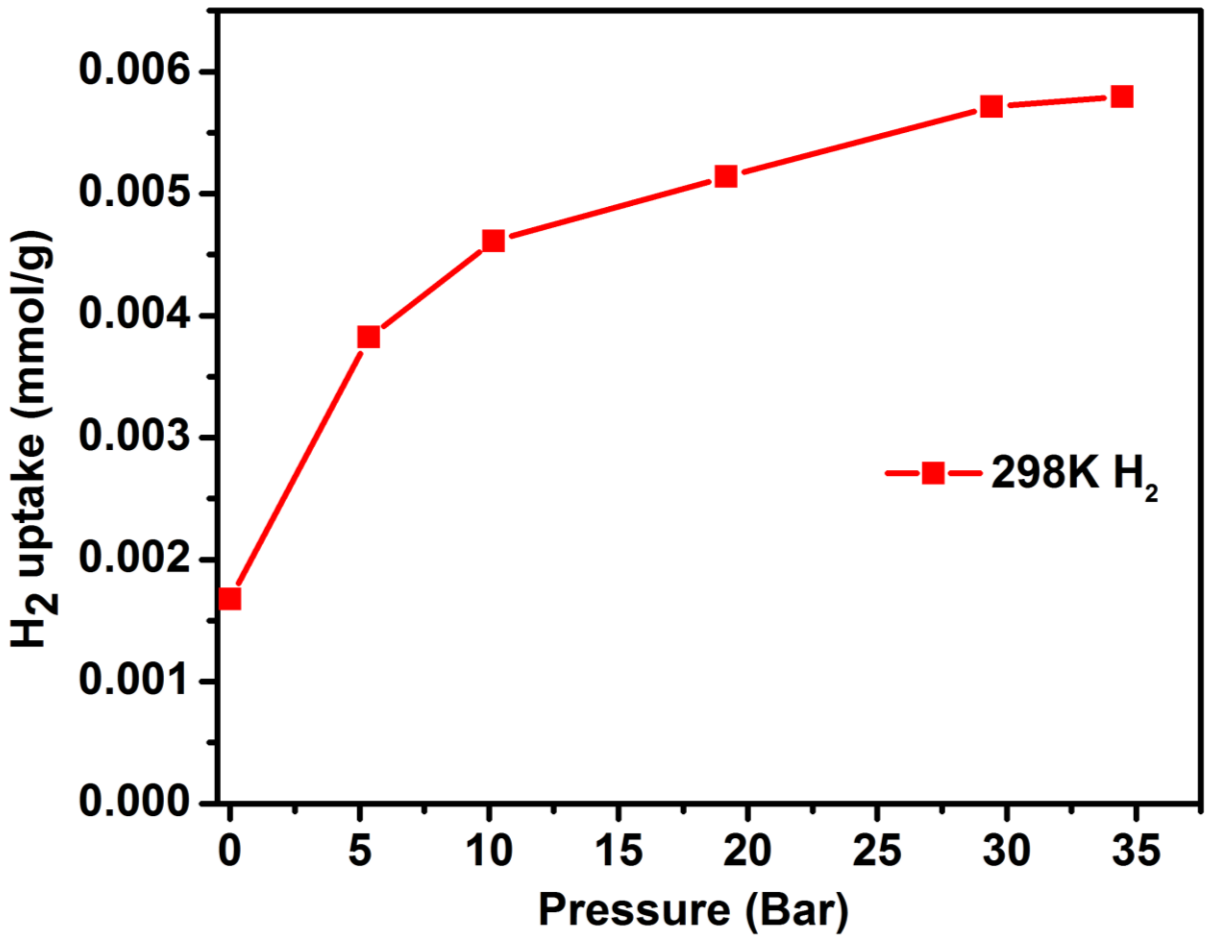

Figure S16. High pressure H_2 isotherm of **1** measured at 298K.

7. Simulation results: HOA, Selectivities, Working capacities

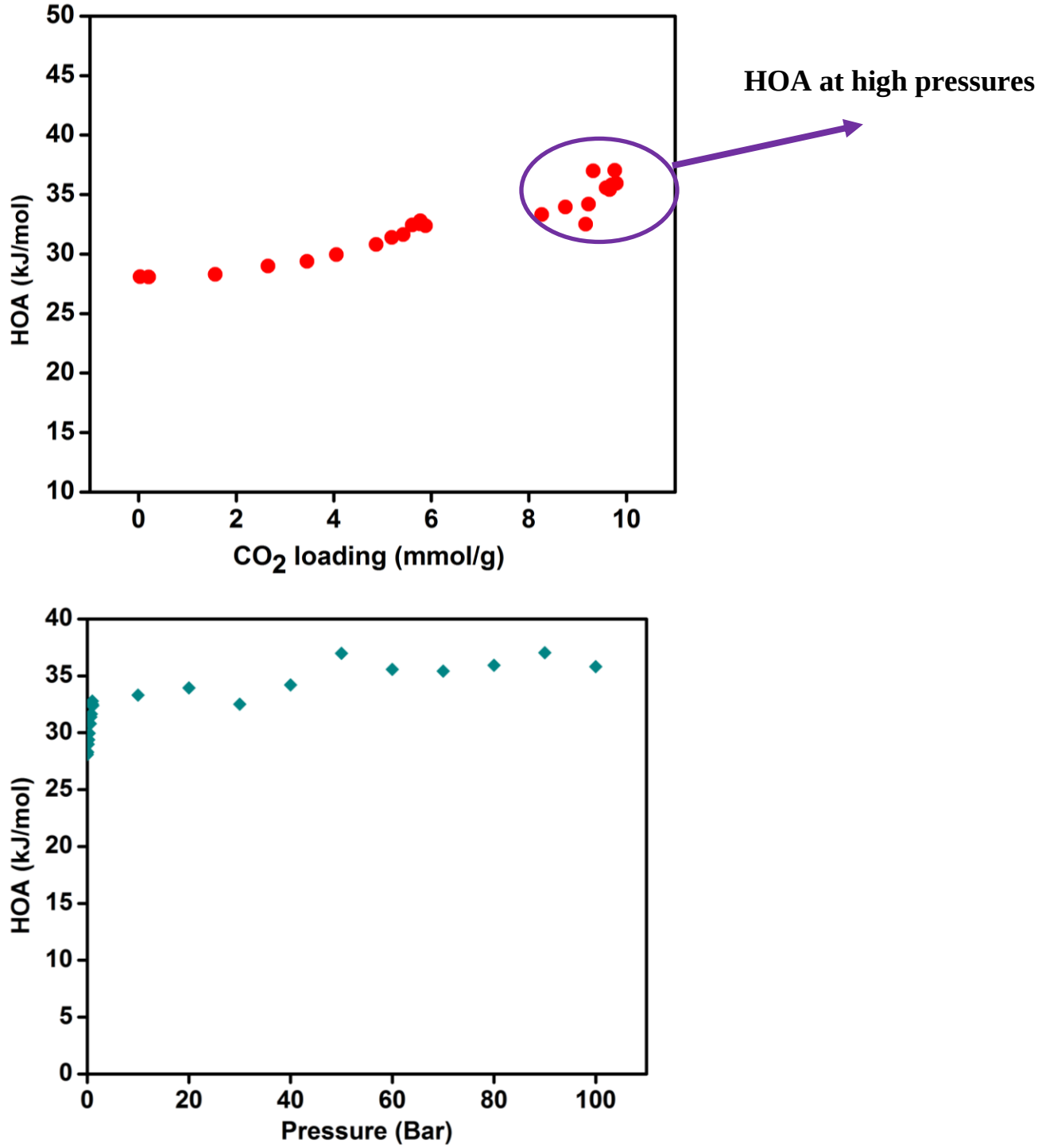

Figure S17. Simulated HOA plots. The HOA climbs up from 28 to 35kJ/mol as we go from ambient to higher pressures. Importantly, the simulations indicate increased CO_2-CO_2 interactions at higher pressures

or around the saturation limit. However, when the CO_2 per unit cell goes beyond the value of 28 molecules/unit cell, they start to interact unfavorably.

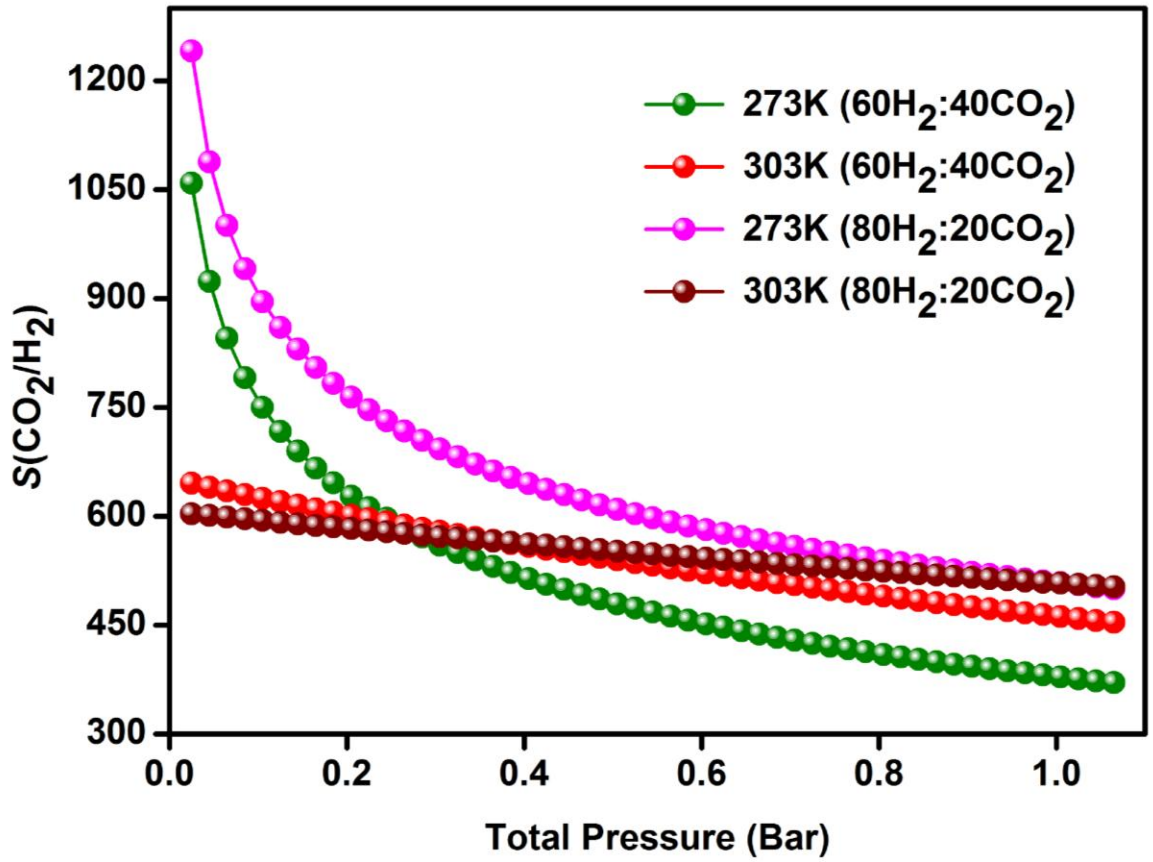

Figure S18. CO_2 selectivity over H_2 calculated using the 273 and 303K pure component adsorption isotherms employing the *IAST* model with a nominal composition of $60H_2$:$40CO_2$ (pre-combustion mix) and $80H_2$:$20H_2$ (H_2 purification mix).

Table S5. Uptakes and selectivities of **1** for the binary CO_2/H_2 (40:60) mixture at relevant ratios for (pre-combustion) gas mixtures and at a range of pressures.

	H_2				**CO_2**			
Temp. (K)	Total Pressure (bar)	Partial Pressure (Bar)	Uptake (mmol/g)	HOA (kcal/mol)	Partial Pressure (Bar)	Uptake (mmol/g)	HOA (kcal/mol)	Selectivity
298	0.1	0.06	0.01	1.916722	0.04	0.74	6.746425	155.23
298	0.5	0.3	0.02	1.934813	0.2	2.63	6.772709	212.56
298	**1**	**0.6**	**0.02**	2.017664	**0.4**	**3.99**	**7.149067**	**255.73**
298	5	3	0.03	2.177165	2	6.64	7.871504	299.35
298	**10**	**6**	**0.04**	**2.266527**	**4**	**7.43**	**8.843813**	**284.01**
298	15	9	0.04	2.389506	6	7.79	7.912919	272.02
298	20	12	0.05	2.981388	8	7.96	9.437865	248.50
298	25	15	0.05	2.292341	10	8.18	8.908687	244.10
298	30	18	0.05	1.559741	12	8.40	7.782887	233.46
298	35	21	0.06	1.866219	14	8.38	7.37276	207.84
298	40	24	0.06	2.261786	16	8.40	7.991161	196.83
313	0.1	0.06	0.01	1.921853	0.04	0.45	6.649933	105.05
313	0.5	0.3	0.02	1.987563	0.2	1.77	6.627739	141.73
313	**1**	**0.6**	**0.03**	**2.011913**	**0.4**	**2.86**	**6.97541**	**168.15**
313	5	3	0.04	2.14258	2	5.86	7.700496	228.55
313	**10**	**6**	**0.04**	**2.724534**	**4**	**6.81**	**8.800282**	**229.29**
313	15	9	0.05	2.253633	6	7.18	8.555156	209.98
313	20	12	0.06	1.926066	8	7.44	7.397351	196.21
313	25	15	0.06	1.938403	10	7.59	8.151489	187.26
313	30	18	0.06	2.111824	12	7.75	8.515188	182.93
313	35	21	0.07	2.213399	14	7.90	8.549941	176.87
313	40	24	0.07	2.758015	16	8.03	9.403098	170.65

Table S6. Uptakes and selectivities of **1** for the binary CO_2/H_2 (20:80) mixture at relevant ratios for (H_2 Purification) gas mixtures and at a range of pressures.

	H2				CO2			
#T/K	Total Pressure	Partial pressure(bar)	Uptake mmol/g	HOA (kcal/mol)	partial pressure(bar)	Uptake (mmol/g)	HOA (kcal/mol)	selectivity
298	0.1	0.08	0.01	1.920102	0.02	0.40	6.735667	166.75
298	0.5	0.4	0.03	1.963284	0.1	1.56	6.852318	238.82
298	**1**	**0.8**	**0.04**	**2.005648**	**0.2**	**2.67**	**6.908323**	**302.96**
298	5	4	0.07	2.048397	1	5.75	7.85293	350.34
298	**10**	**8**	**0.07**	**2.074195**	**2**	**6.69**	**7.356118**	**409.13**
298	15	12	0.08	2.243754	3	7.04	7.623559	359.52
298	20	16	0.08	2.108895	4	7.36	8.261807	353.53
298	25	20	0.09	1.776085	5	7.51	8.351958	327.75
298	30	24	0.09	2.133306	6	7.85	7.918106	336.14
298	35	28	0.11	2.199715	7	7.77	8.343457	289.47
298	40	32	0.11	1.239039	8	7.89	6.465226	286.11
313	0.1	0.08	0.01	1.94776	0.02	0.24	6.660496	111.58
313	0.5	0.4	0.03	1.972521	0.1	1.02	6.764387	162.14
313	**1**	**0.8**	**0.04**	**2.000007**	**0.2**	**1.76**	**6.703865**	**194.51**
313	5	4	0.08	1.923165	1	4.66	6.985618	233.05
313	**10**	**8**	**0.08**	**2.107586**	**2**	**5.80**	**7.90553**	**285.51**
313	15	12	0.09	2.23058	3	6.43	8.130206	293.01
313	20	16	0.10	2.033347	4	6.76	7.562858	278.76
313	25	20	0.11	2.754483	5	7.01	9.073617	265.68
313	30	24	0.11	2.423217	6	7.15	8.690889	249.17
313	35	28	0.12	2.050799	7	7.27	8.064731	249.39
313	40	32	0.13	2.1477	8	7.33	8.162616	219.81

Table S7. Working capacities and selectivities for a PSA from 10 bar to 1 bar at 313 K at the relevant H_2/CO_2 gas mixtures for H_2 purification (80:20) and precombustion CO_2 capture (60:40) for integrated gasification and combined cycle (IGCC) systems.

Material	H_2 Purification Working Capacity (mol/kg)	H_2 Purification Selectivity	Precombustion CO_2 Capture Working Capacity (mol/kg)	Precombustion CO_2 Capture Selectivity
Ni-4PyC	4.05	285	3.95	229
Activated Carbon JX101	1.90	94	3.00	75
Zeolite 13x	2.20	320	1.90	250
Mg_2(dobdc)	3.20	610	4.00	450
Cu-BTTri	3.00	31	5.00	28

Calculation of working capacity based on 313K mixed component isotherm for 10bar to 1bar PSA:

Working Capacity: This is a measure of how much carbon dioxide adsorbs from a gas mixtures in an adsorption unit over a given pressure swing. With a standard 40:60 and 20:80 CO_2:H_2 mix-component isotherm @ 313K and a pressure swing of 10bar to 1bar yields a working capacity of 4.1 and 3.95 mmol g-1 respectively.

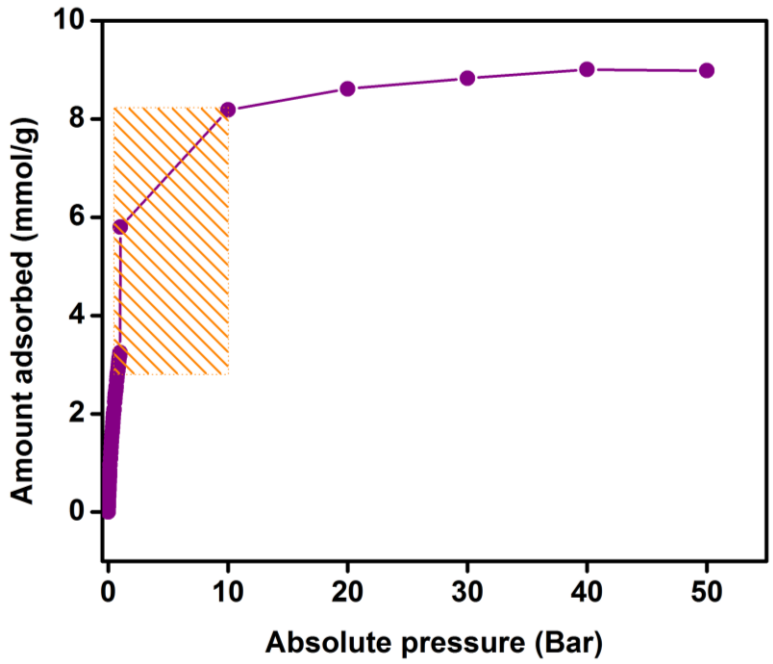

Figure S19. Working capacity 5.0 mmol/g for a PSA (10bar to 1bar) at 298K for the pure component.

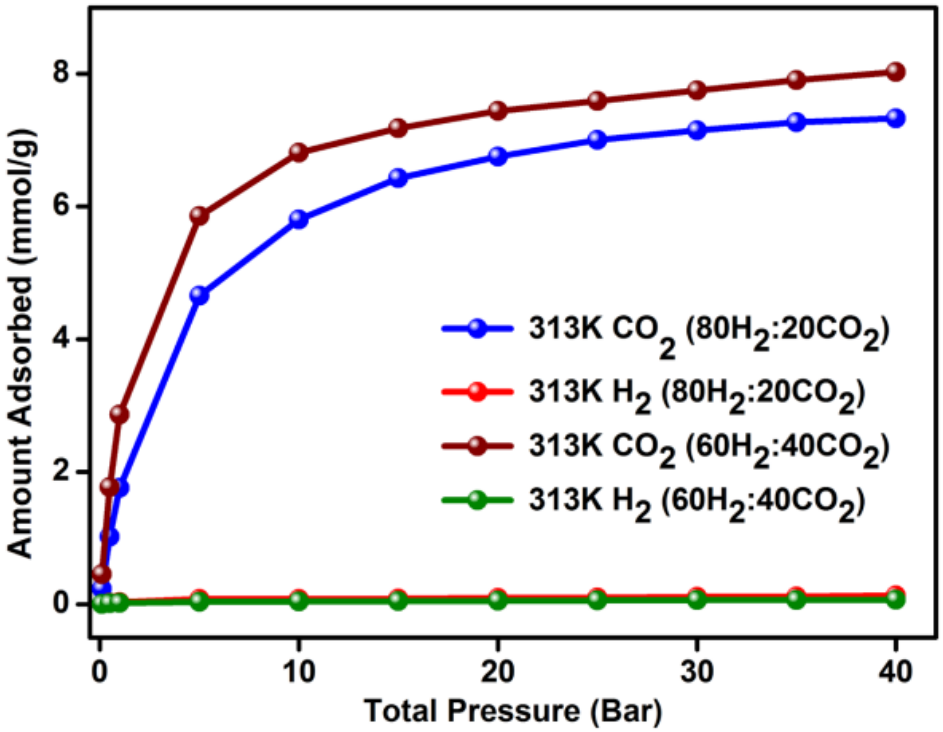

Figure S20. Isotherms simulated from a hydrogen purification ($80H_2$:$20CO_2$) and pre-combustion mixture ($60H_2$:$40CO_2$).

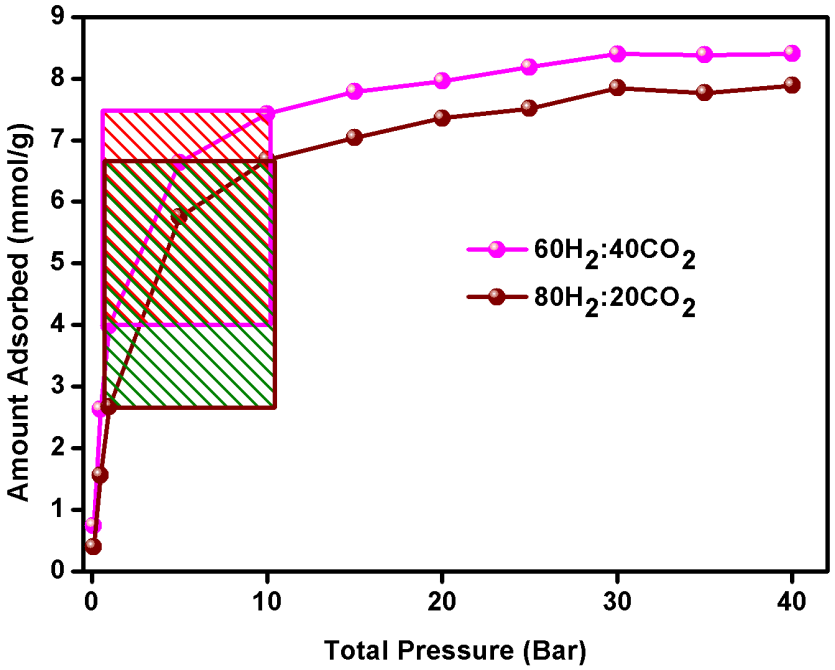

Figure S21. Working capacity for a PSA (10bar to 1bar) at 298K for the gas mixture with $60H_2$:$40CO_2$ and $80H_2$:$20CO_2$.

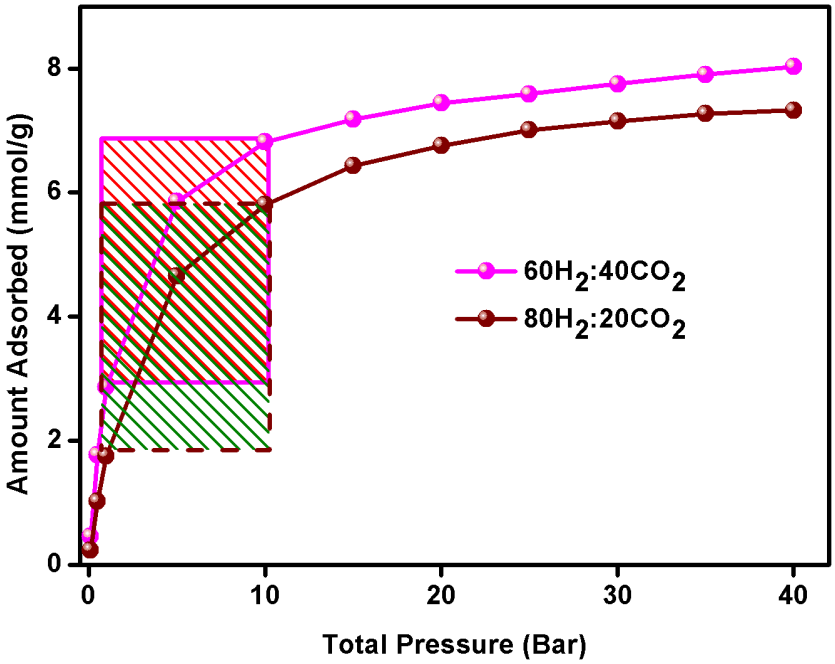

Figure S22. Working capacity for a PSA (10bar to 1bar) at 313K for the flue gas mixture with $60H_2$:$40CO_2$ and $80H_2$:$20CO_2$.

8. Stability studies

Mentioned in this section are some of the important requirements for any MOF when it comes to its potential industrial application. These ultra and microporous MOFs are quite interesting owing to their good stability to solvent removal as compare to the large pore MOFs which in many cases require highly demanding moisture free handling and in spite of that tend to show partial to complete loss of long range order. **1** has excellent shelf-life and they retain complete porosity even after 6 months. Additionally, the hydrolytic stability of the material was confirmed by exposing the material to steam for over 7 days. **1** loses < 5% porosity after 2 days (calculated from 77K N_2 and 195K CO_2 isotherms) and no further loss was observed even after 7 days.

To substantiate the stability of the material not only from crystallinity, but further from the intactness of porosity, we have carried out gas adsorption studies on samples subjected to operational conditions (Figs. S26-S29). Having had suggested the potential use of **1** at high pressures it becomes important to weigh up the hydrostatic stability of **1**. Many MOFs have been reported to lose substantial amount of their porosity due to amorphization at high pressures.(Ref 43 of main text) When **1** was subjected to ~70bar (0.5 tons) for about 24hrs and it did not show any amorphization as evidenced from the PXRD and gas adsorption (Fig. S28).

We believe that when proposing a MOF for as an solid adsorbent for gas capture applications it is important to evaluate its gas uptakes across multiple syntheses and across repeated adsorption-desorption cycles, however **1** showed excellent synthetic homogeneity across batches and also good repeatability of its CO_2 uptake as evidenced from the adsorption studies and cycling studies from TGA. PXRD studies indicate the complete retention of crystallinity after nearly 16 cycles of CO_2 and N_2 adsorption followed by exposing to atmosphere for a month. Retaining such high degree of crystallinity in large pore MOFs could be tricky. In

addition, **1** could be scaled-up to 10gm with ease and the product showed comparable crystallinity and similar gas sorption characteristics (Figs. S3 and S7).

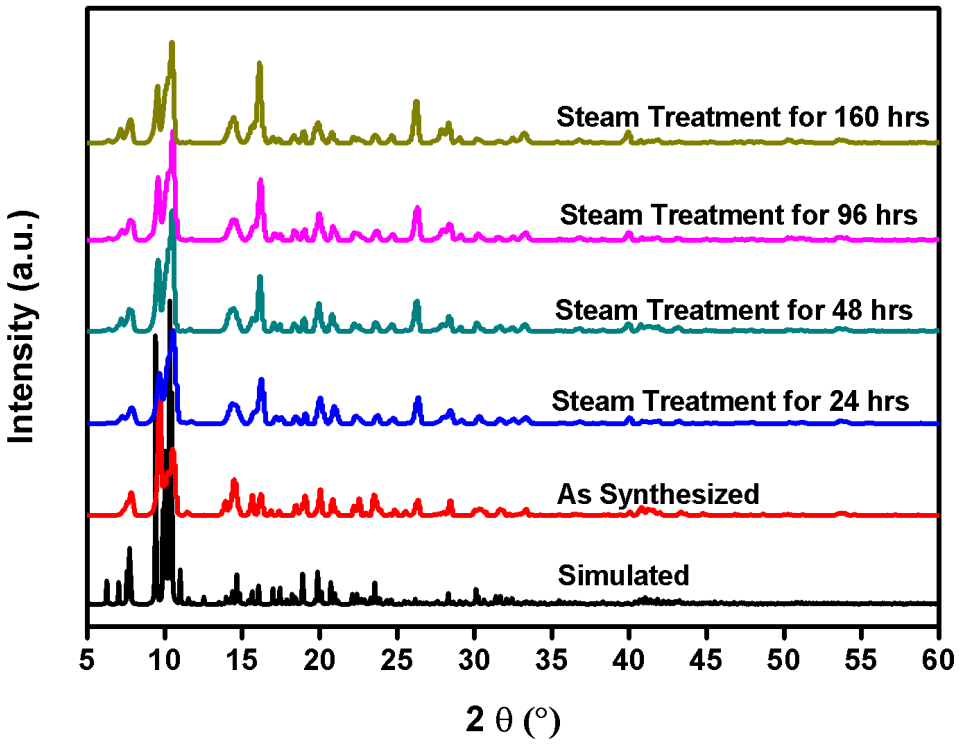

Figure S23. PXRD comparisons of the as-made sample with the simulated. Presented is also the PXRDs indicating the hydrolytic stability of **1**.

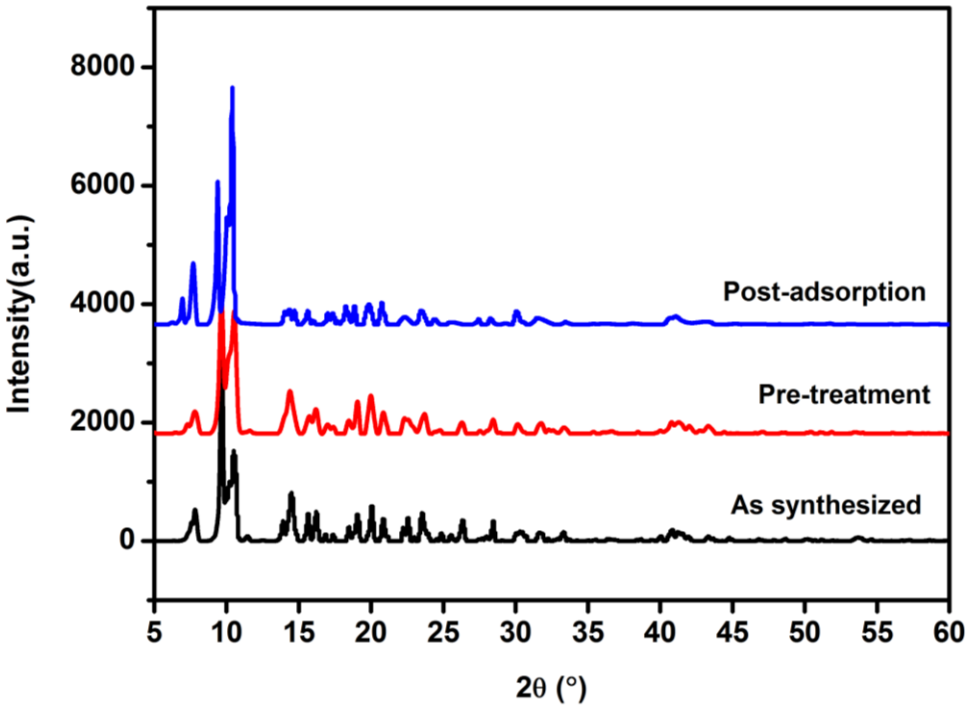

Figure S24. Comparison of PXRDs indicating the complete retention of crystallinity following repeated (~8-10 cycles) heating and cooling of **1** during multiple gas adsorption studies.

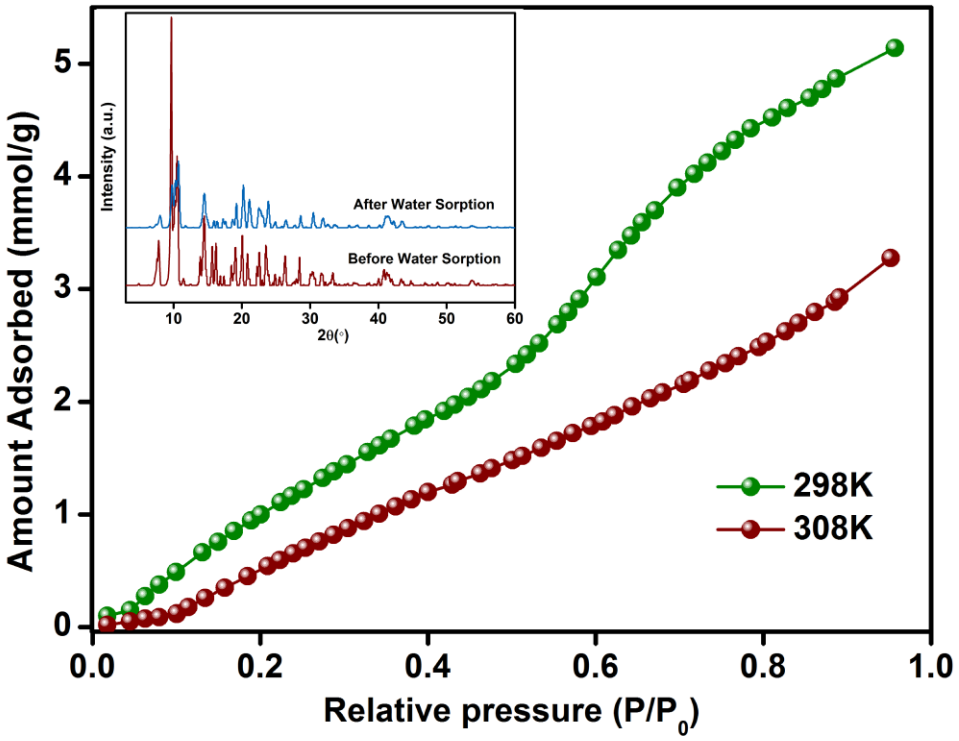

Figure S25. The water adsorption isotherm carried out on **1** at 298K. Inset showing the PXRD of the post adsorption phase. Both together represent the hydrolytic stability of **1**.

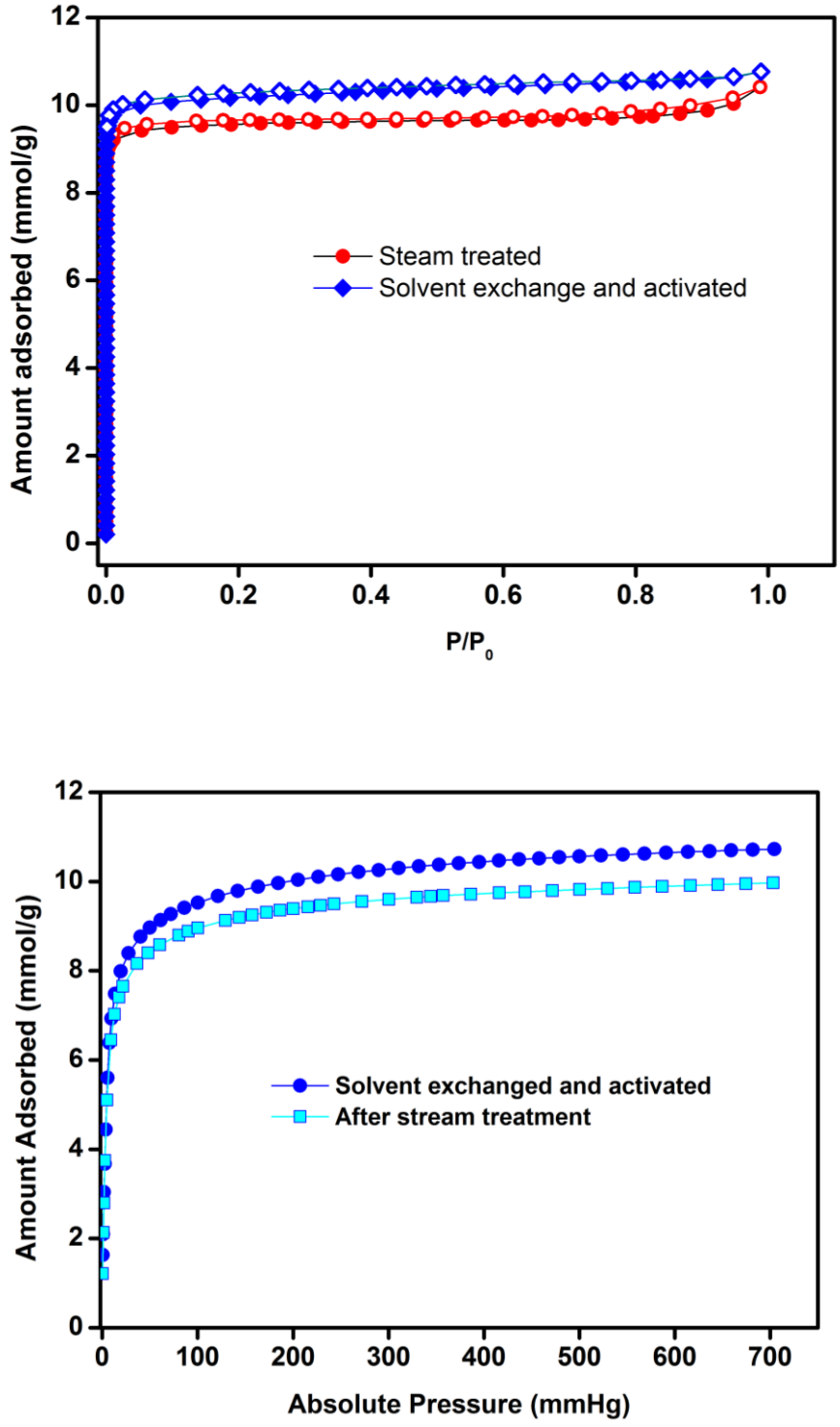

Figure S26. Hydrolytic stability of **1**. Top: Comparison of the N_2 adsorption at 77K for the freshly activated sample and the sample that was exposed to >95% steam for ~7days. Bottom: Comparison of the CO_2 adsorption at 195K for the freshly activated sample and the sample that was exposed to >95% steam for ~7days.

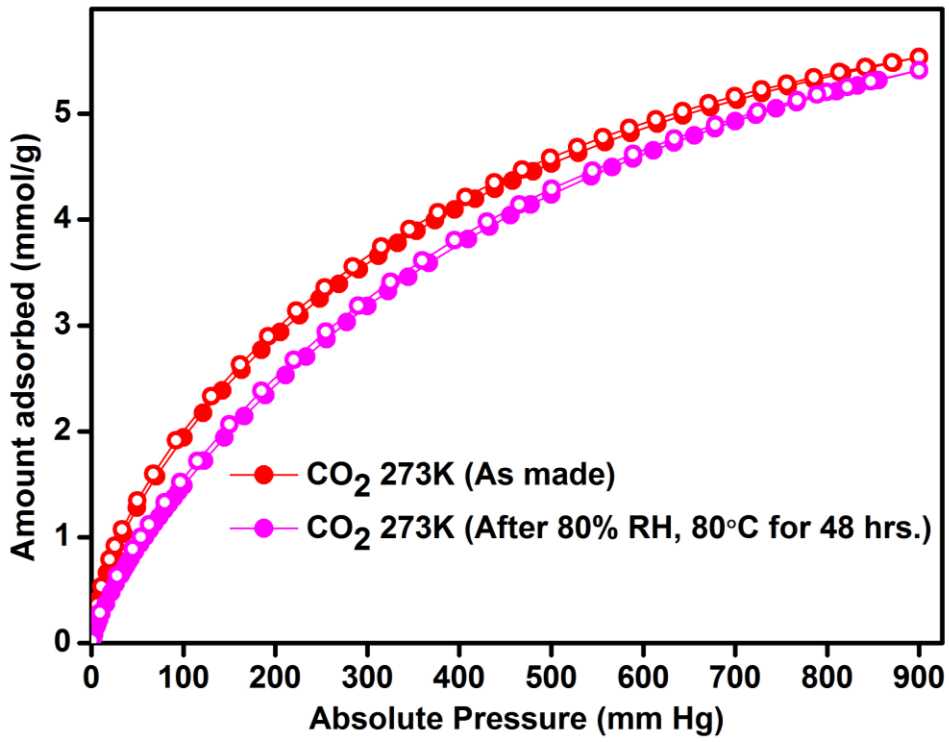

Figure S27. The comparison of the CO_2 adsorption isotherms of **1**, as made (red) vs sample exposed to 80%RH at 80^{o}C for 48hrs (magenta).

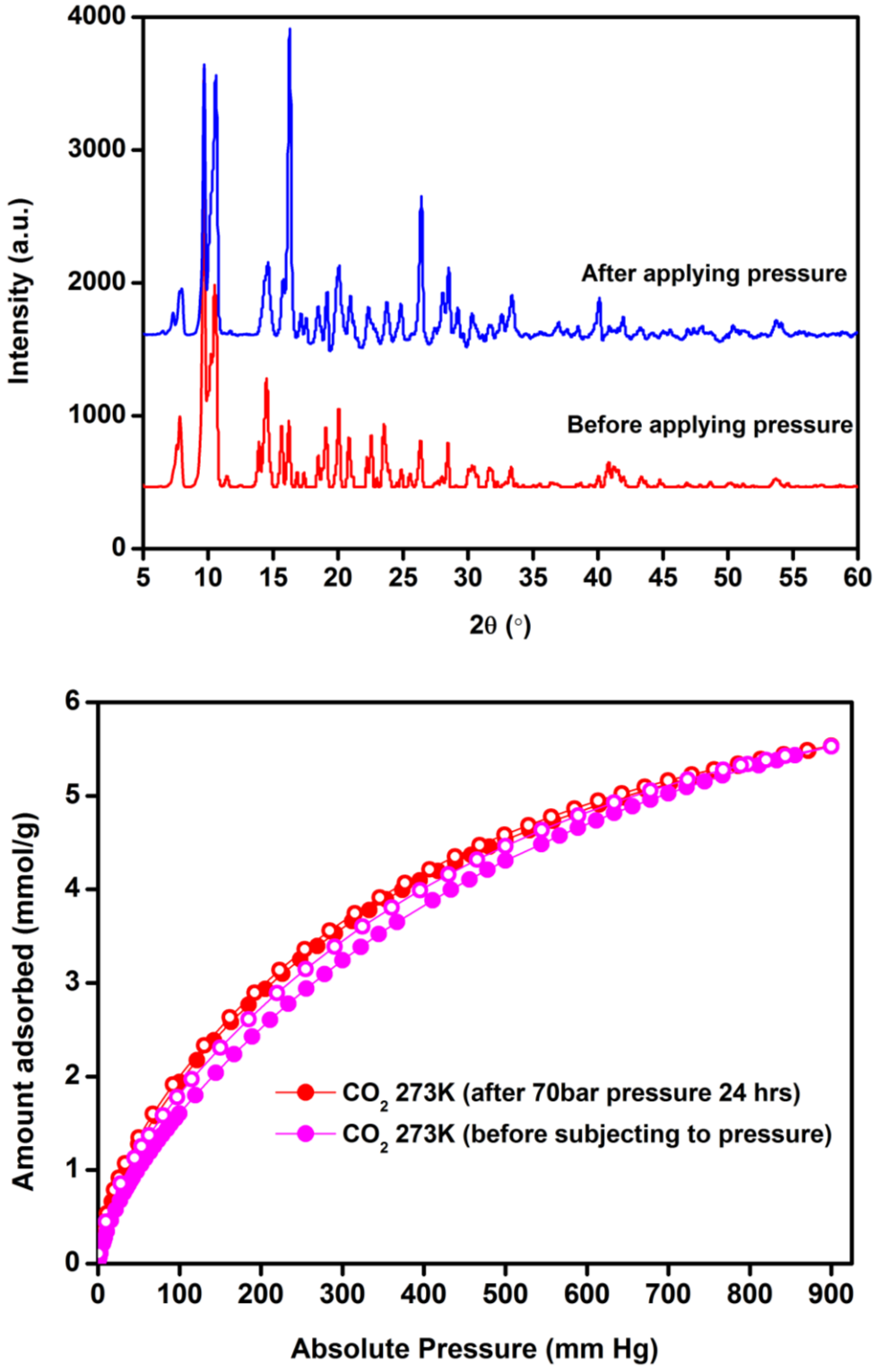

Figure S28. Pressure induced amorphization test for **1**. Note there is hardly any loss in crystallinity or gas uptake. Pressure of 70bar is twice what is industrially used.

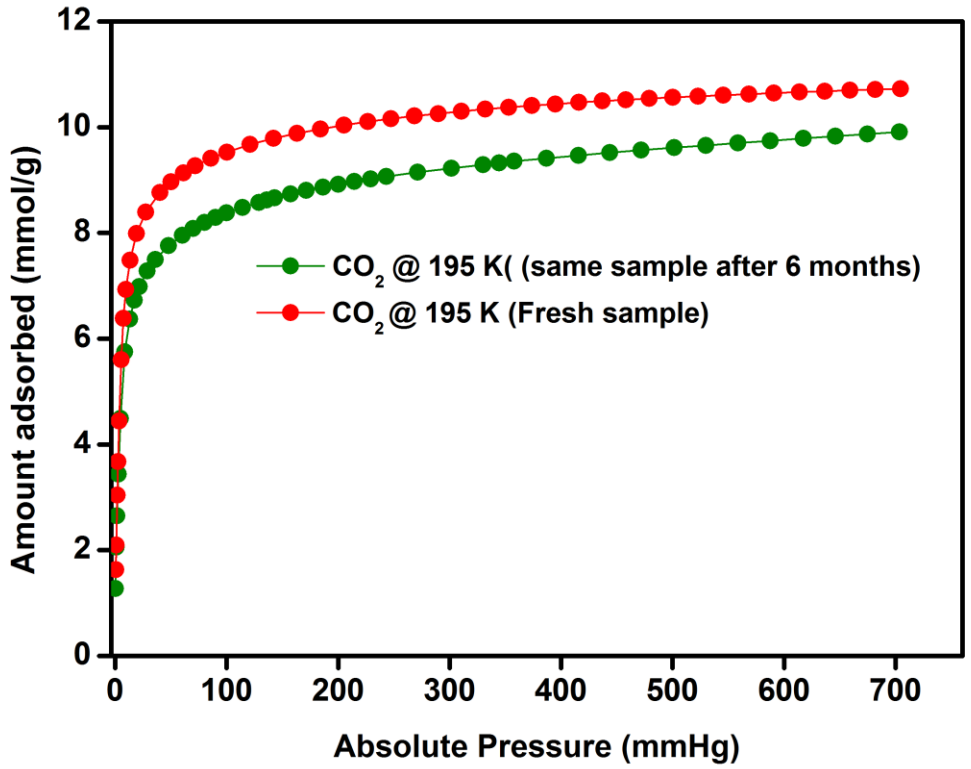

Figure S29. The comparison of the CO_2 adsorption in **1** between a freshly prepared phase and one that has been sitting in a bottle for over 6 months.

9. Adsorption-Desorption Cycling Experiments

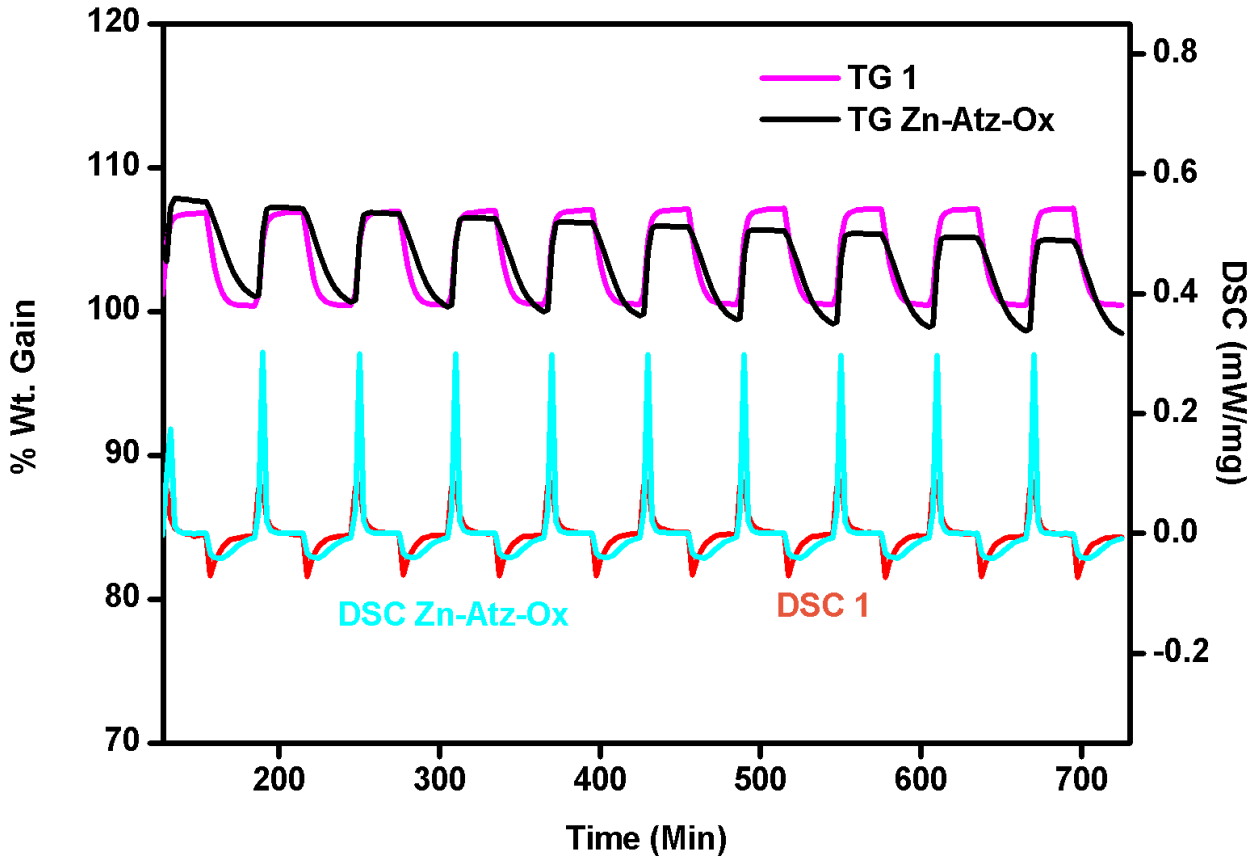

Figure S30. TGA cycling data for CO_2-N_2 cycling done on **1** and ZnAtzOx at 35°C. N_2 and CO_2 were flowed at 20ml/min and each cycle starts with a CO_2 (30mins) followed by a N_2 (30mins). Both **1** and ZnAtzOx show ~6.5% Wt. gain. Comparison of the DSC trace indicates the higher heat of adsorption for the latter as would be expected (HOA: 28kJ/mol for 1 vs. 40kJ/mol for ZnAtzOx). Also, a closer look at the profiles of the TG shows the facile removal of the CO_2 in **1**, as compared to ZnAtzOx as indicated by the sharper desorption for **1**. The drift in the TGA with time in the case of ZnAtzOx is entirely due to baseline issues, the weight gain remains unchanged between cycles.

10. Self-diffusion coefficient CO_2 in 1:

Diffusion coefficient determination from Rate of adsorption measurements: An extremely high resolution rate of adsorption measurement was carried out using the ASAP2020HD instrument at 273K in the pressure range of 0-1bar. The diffusion coefficient was calculated as a function of CO_2 loading. For this purpose, 8 different loading points (N= 1.09, 1.67, 2.17, 2.60, 2.99, 3.31, 3.63 and 3.93) were used and each of the ROA data was fitted to a spherical pore model (Kourosh et al. *J. Chem. Phys.*, 119, 2801 (*2003*); Adsorption analysis and equilibria and kinetics, D. D. Do, Imperial College Press, Ed. 2008):

$$F = 1 - \frac{6}{\pi^2} \sum_{n=1}^{\infty} \frac{1}{n^2} \text{Exp}(-n^2 \pi^2 \tau)$$

F = fractional uptake; τ = non-dimensional time given by $\tau = Dt/R^2$, where R= particle size; t= time (secs); D = apparent diffusivity.

The single-component diffusion coefficient was estimated to be $3.08 \times 10^{-9} m^2 s^{-1}$ taking the average of these eight points. Note: the kinetics of the low loadings (<1mmol/g) were extremely hard to model.

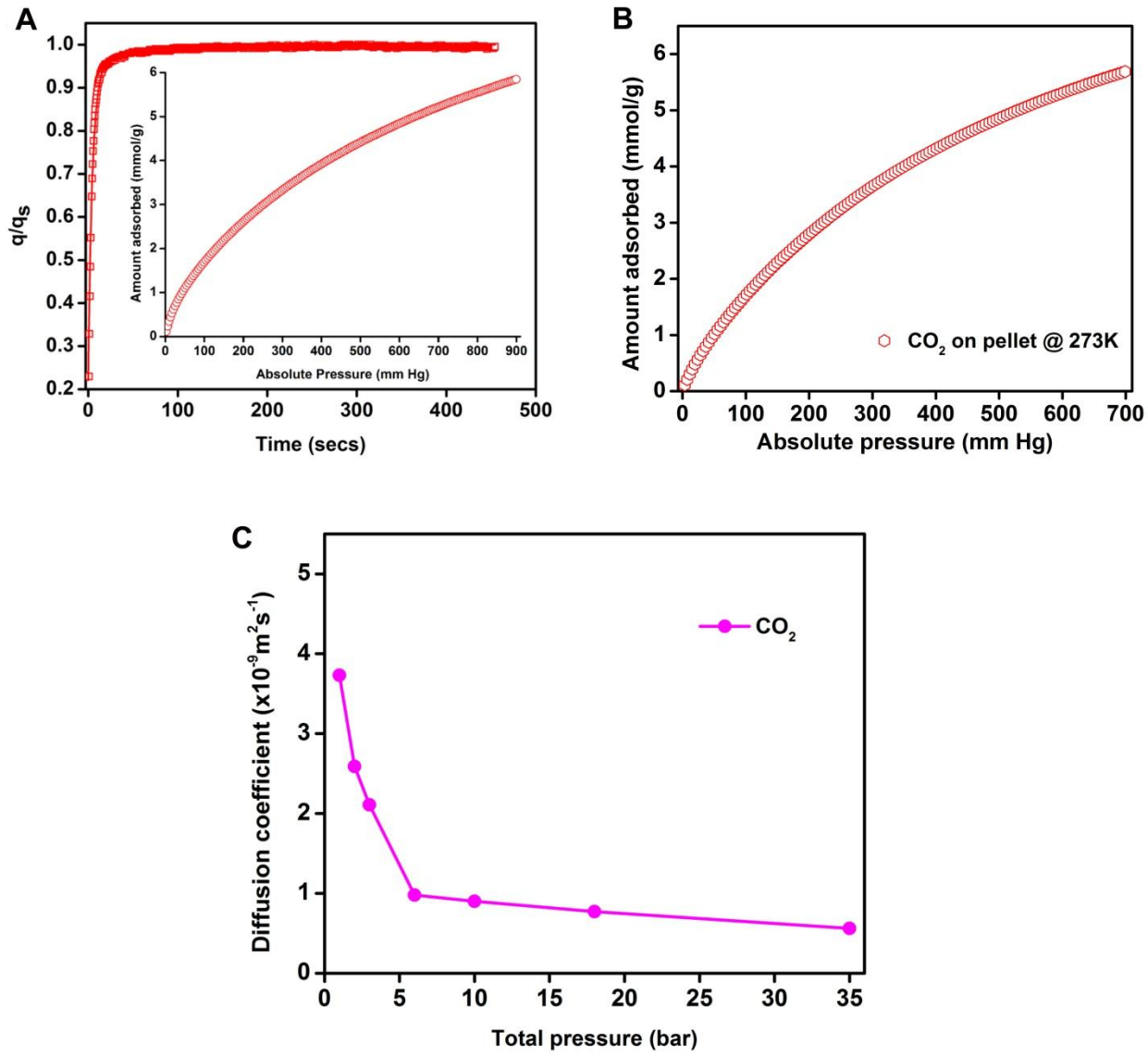

Figure S31. Top: Representative plot of the adsorbate fractional filling vs. time showing the fit between the spherical model (line) and the collected data (spheres) obtained from the single component CO_2isotherm. Inset shows the high resolution 273K adsorption isotherm used in this diffusion modeling. Note nine such fittings were considered to obtain the average diffusion coefficient. Bottom: Self-diffusion coefficient for CO_2 obtained from simulation studies.

11. Computational and Molecular Modeling Details

The simulated uptake of Ni-4PyC was calculated using Grand Canonical Monte Carlo (GCMC) calculations. Both single component and binary mixtures of CO_2 and H_2 were performed. The initial experimental crystal structure of **1** had disorder with respect to the orientation and direction of the organic SBU. The SBU could either bind the metal centre via the nitrogen of the pyridine ring or the oxygen of the carboxylic acid, which resulted in the observed disorder. Of all possible combinations of the organic SBU orientations, only three had no serious steric overlap. These three structures had almost identical isotherms with the greatest difference in uptake being only 0.1 mmol/g through the pressure range from 0-1 bar. The structure with the least symmetry was used. Before GCMC calculations could be performed, the MOF framework structure was optimized using periodic density functional theory (DFT) (P. Hohenberg, *Phys. Rev.* 136, B864 (1964); W. Kohn, et al. *Phys. Rev.* 140, A1133 (1965)). Geometry optimizations were performed starting from high quality experimental X-ray structures with all atoms and unit cell parameters optimized. Periodic DFT calculations were performed with the VASP code (G. Kresse et al., *Phys. Rev.* B 47, 558 (1993); *Phys. Rev.* B 54, 11169 (1996)) using the PBE exchange-correlation functional (J. P. Perdew et al. *Phys. Rev. Lett.* 77, 3865 (1996)). PAW pseudopotentials (P. E. Blöchl, *Phys. Rev. B* 50, 17953 (1994); G. Kresse, *Phys. Rev. B* 59, 1758 (1999))were used in a plane wave basis set with a kinetic energy cut-off of 520 eV. All calculations were spin polarized and only the Γ-point was sampled. Empirical dispersion corrections of Grimme (S. Grimme, *J. Comput. Chem.* 27, 1787 (2006)) were included in both energy and force calculations with the default scaling factor of 0.75, as parameterized by Grimme, for the PBE functional.

GCMC calculations were performed with the framework held fixed while the gas guest molecules were assumed to be rigid. The electrostatic energetic contributions were determined by partial atomic charges assigned to each atom calculated with the REPEAT method (C. Campañá et al. *J. Chem. Theory Comput.* 5, 2866 (2009)) using the DFT derived electrostatic potential. Dispersive and steric repulsive interactions were included by a 12-6 Lennard-Jones (L-J) potential for each atom. The ε and σ parameters for the framework were taken from the Universal Force Field (UFF) (A. K. Rappe et al. *J. Am. Chem. Soc.* 114, 10024 (1992)). H_2 Lennard-Jones parameters, the H-H bond length (0.742 Å), and point charges for the five-site H_2

model were taken from work by Belof *et. al* (*J. Chem. Theory Comput.* 4, 1332 (2008)) which is a hydrogen potential for condensed phase simulation. These parameters have been used in the simulation of H_2 in to study the adsorption of H_2 in ultra-microporous MOFs (K. A. Forrest, *J. Phys. Chem. C* 117, 17687 (2013)) and are shown below in table S8.

Table S8. Forcefield parameters for the 5-site H_2 model taken from by Belof *et. al* (2008). H2E corresponds to the true atomic positions of hydrogen atoms, H2G coincides with the center-of-mass site, and H2N contains the additional Lennard-Jones sites.

Atom	R / Å	Q / e	ε / kcal mol^{-1}	σ / Å
H2E	-0.371	0.3732	0.0000000	0.0000
H2N	-0.329	0.0000	0.0080798	2.3406
H2G	0.000	-0.7464	0.0175899	3.2293
H2N	0.329	0.0000	0.0080798	2.3406
H2E	0.371	0.3732	0.0000000	0.0000

The ε and σ parameters of CO_2 were taken from García-Sánchez *et al.* (*J. Phys. Chem. C* 113, 8814 (2009)) which were developed to fit experimental adsorption isotherm data in zeolite frameworks. The C-O bond length (1.149 Å) and partial charges on CO_2 atoms (C = +0.6512*e*, O = -0.3256*e*) were taken from the potential by Harris and Yung (*J. Phys. Chem.* 99, 12021 (1995)). Lennard-Jones parameters of all atom types are given in table S9.

Table S9. Lennard-Jones parameters for framework atoms from the UFF forcefield, CO_2 guest molecules.

Forcefield	Atom	ε / kcal mol^{-1}	σ / Å
UFF	C	0.1050	3.4309
UFF	O	0.0600	3.1181
UFF	N	0.0690	3.2607
UFF	Ni	0.0150	2.5248
García-Sánchez *et al.*	O (CO_2)	0.1702	3.0170
García-Sánchez *et al.*	C (CO_2)	0.0595	2.7450

GCMC simulations were performed with an in-house code. The number of production steps used was 10^7 after an initial equilibration stage of 10^6 steps for each gas pressure point on

the isotherm. The Monte Carlo algorithm utilized equal probabilities for the moves of guest displacement, insertion, and deletion. A cut-off of 12.5 Å was used for long range interactions which were calculated using a Ewald summation. For pressures less than 1 bar, the ideal gas pressure was used in the Monte Carlo guest insertion and deletion criteria. Conversely, pressures greater than 1 bar was corrected for fugacity by evaluating the uptake based on pressures fitted to the Peng-Robinson Equation of State. (R. Stryjek et al. *Can. J. Chem. Eng.* 64, 323 (1986)). A 2x2x3 super-cell was used for the GCMC simulations. A similar approach has been used by us successfully to analyze CO_2 binding within an amine-functionalized MOF (Ref. 32 of main text).

From the probability distributions generated via the GCMC simulations the most probable CO_2 binding sites were calculated. The in-house code uses a Gaussian filter to smooth the GCMC probabilities. From here the maxima in the smoothed probability is determined. A single atom is fitted to this maxima and then the molecule is built such that the orientation fits maxima in the probability distributions of the other atom types in the molecule. The geometry was then optimized using the DL_POLY package (T. R. Forrester et al. DL_POLY ver. 2.18 (C.L.R.C. Daresbury Laboratory, Daresbury, UK, 1995)) with 200 MD steps at zero Kelvin. The ranking of binding sites were based on interaction energy and the occupancy of the binding sites with respect to the probability distributions. For determination of the binding energies, single point calculations were performed with interaction energies subdivided into dispersion and electrostatic contributions. The binding energy per CO_2 molecule is defined as,

$$E_{binding} = E(\mathrm{MOF} + n\mathrm{CO_2}) - E(\mathrm{MOF}) - nE(\mathrm{CO_2}) \quad \text{(S1)}$$

where the configurational energies for the MOF with the guest CO_2included in the simulations are used for $E(\mathrm{MOF} + n\mathrm{CO_2})$. $E(\mathrm{MOF})$is the configurational energy of the MOF with no guests. $nE(\mathrm{CO_2})$is the configurational energy of one CO_2 molecule times *n* number of CO_2 molecules. The cooperative energy was calculated as,

$$E_{cooperative} = E(\mathrm{MOF} + n\mathrm{CO_2}) - E(\mathrm{MOF} + (n-1)\mathrm{CO_2}) \quad \text{(S2)}$$

where the configurational energy of the MOF with *n* number of CO_2 molecules in the unit cell is $E(\mathrm{MOF} + n\mathrm{CO_2})$. The term $E(\mathrm{MOF} + (n-1)\mathrm{CO_2})$ is the summation of the binding energies of *n-1* number of CO_2 molecules in the unit cell as such,

$$\sum_{i=1}^{n-1} E(\mathrm{MOF} + n\mathrm{CO_2}) - E(\mathrm{MOF}) - nE(\mathrm{CO_2}) \quad \text{(S3)}$$

A summary of cooperative binding energies of the 9 least ranked binding site CO_2 molecules is shown in table S10.

Table S10. Cooperative CO_2-CO_2 energies with respect to the number of molecules loaded.

n CO_2 per unit cell	Total Cooperative Energy (kJ/mol)	Cooperative Energy Per CO_2(kJ/mol)
22	-108.7	-4.9
23	-118.5	-5.1
24	-120.0	-5.0
25	-121.2	-4.8
26	-123.8	-4.8
27	-136.3	-5.0
28	-146.6	-5.2
29	-152.9	-5.3
30	-145.3	-4.8

Molecular dynamics simulations were performed with DL_POLY in order to calculate the diffusion coefficients. The diffusion coefficients were determined from a single time origin from the calculated mean-square displacement (MSD) over time. The MSD is calculated as an average property of all *N* CO_2 molecules as,

$$MSD(t) = \frac{1}{N}\langle \sum_{i=1}^{N} |\boldsymbol{r_i}(t) - \boldsymbol{r_i}(0)|^2 \rangle = \langle |\boldsymbol{r}(t) - \boldsymbol{r}(0)|^2 \rangle \quad \text{(S5)}$$

where $r_i(0)$ corresponds to a starting position at time t = 0 and $r_i(t)$ corresponds to a position at time t. The diffusion coefficient, *D*, is defined as the slope of MSD with respect to time,

$$\lim_{t\to\infty} \frac{d\langle|\boldsymbol{r}(t)-\boldsymbol{r}(0)|^2\rangle}{dt} = 6D \qquad \text{(S6)}$$

The MD simulation was done at 298.15 K and 1 bar with 0.2 ns of equilibration, 1 ns for the production run, and a time step of 0.001 ps with an NVT ensemble. This was done at flue gas conditions with a binary mixture of $15CO_2$:$85N_2$ in a 2x2x3 supercell with 69 CO_2 molecules which corresponds to a 2.10 mmol/g loading. A graph of the MSD with respect to time is shown in Figure S32.

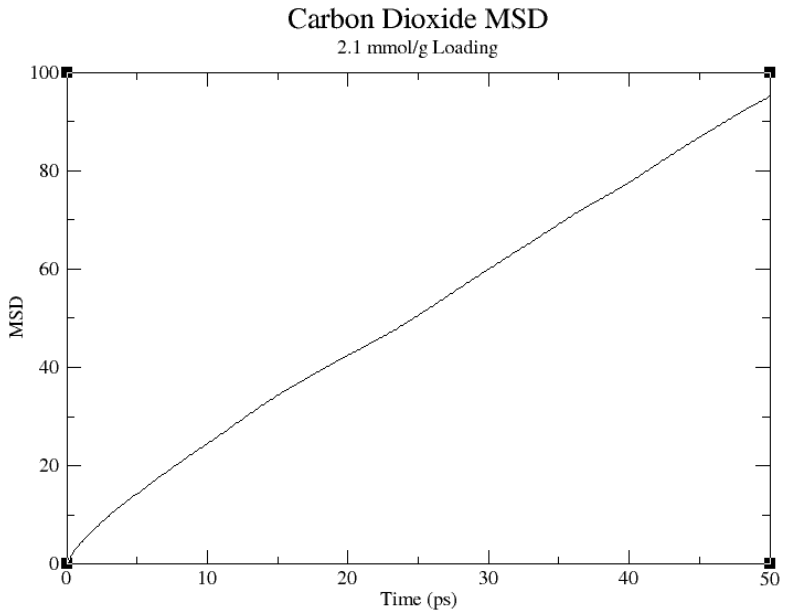

Figure S32. Plot of the Mean Square Displacement (MSD) as a function of time resulting from a molecular dynamics simulation of CO_2 in **1** at 298.15 K and 1 bar with a loading of 2.1 mmol/g.

The void volume (0.0434 cm^3/g) and surface area (1193.16 m^2/g) were calculated using the Zeo++ code (T. F. Willems et al. *Microporous Mesoporous Mater.* 149, 134 (2012); R. L. Martin, *J. Chem. Inf. Model.* 52, 308 (2012)) with a probe radii (1.72 Å) corresponding to CO_2 gas molecules. The accessible volume as measured by a solvent probe radius of 1.72 Å shows the presence the 1D channels which running through the unit cell. The center pore was found to be accessible via the channels at 1.00 Å which was also found to contain the strongest binding sites as mentioned in the main text. Depending on the orientation of the CO_2 molecule, it should be able to access this pocket via the channels. A graphical representation of the accessible volume is shown in figure S33.

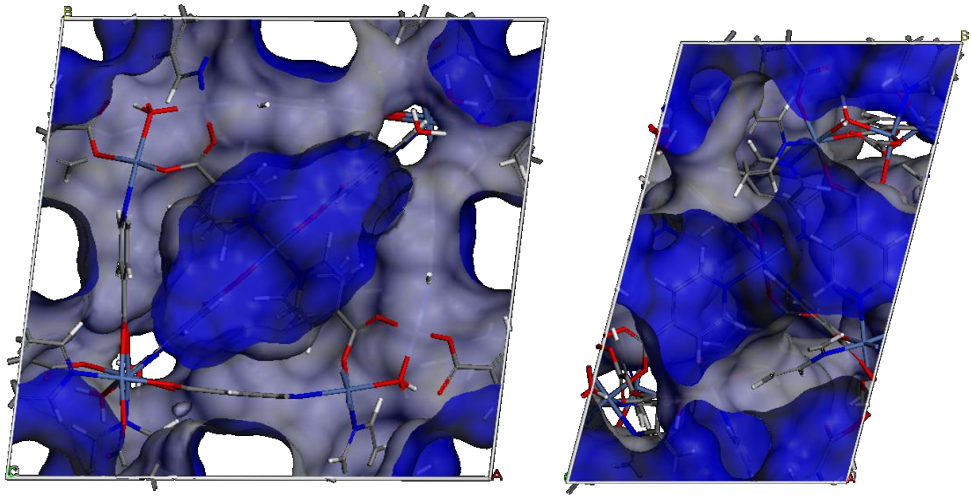

Front View Side View

Figure S33. A graphical representation of the accessible volume of **1** with a probe radii of 1.41 Å.

In order to validate whether the CO_2 molecules are accessible to the middle cage, molecular dynamics simulations were performed with DL_POLY. Two configurations were tested, one where the channels were saturated and the cage was empty and vice versa. This was done at 313 K and 10 bar to model high pressure adsorption with 0.2 ns of equilibration, 1 ns for the production run, and a time step of 0.001 ps with an NVT ensemble. In both simulations the CO_2 molecules diffuse into and out of the cages. It was found that cage to channel diffusion occurred throughout the simulation time length while channel to cage diffusion occurred almost instantaneously. Snapshots of the simulation are showed in Figure S34.

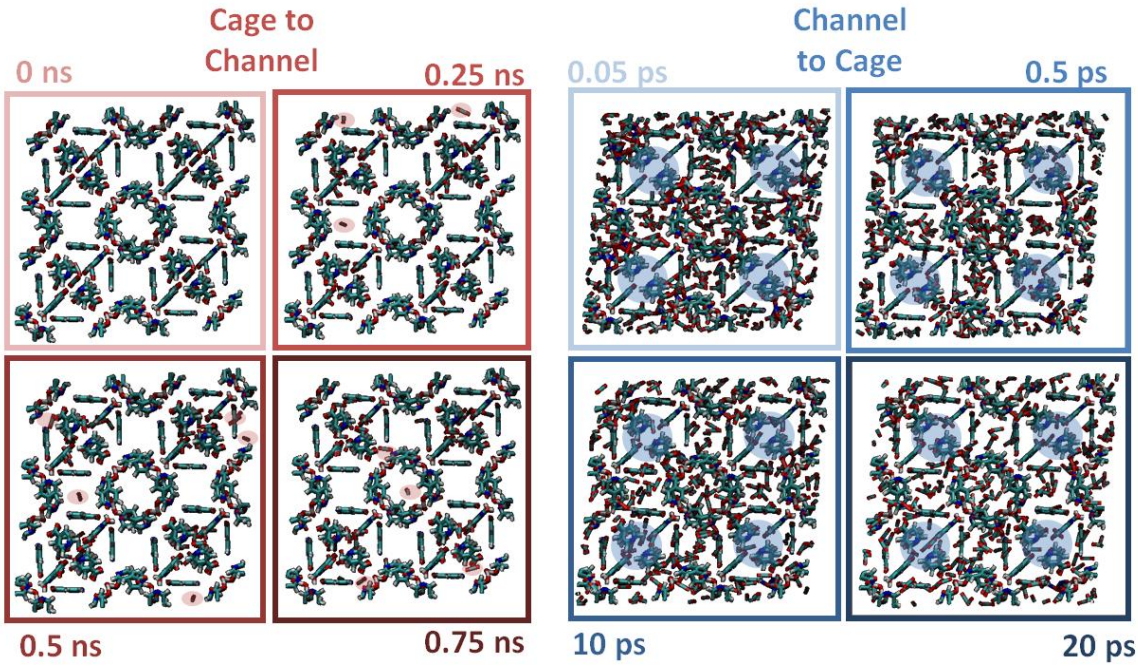

Figure S34. Snapshots from the MD simulation of CO_2 diffusing from the cage to the channel and vice versa. Highlighted in red are the CO_2 molecules which have diffused from the cage to the channel and highlighted in blue are the cages with CO_2 molecules inside. This was visualized using VMD (W. Humphrey, *J. Mol. Graph.* 14, 33 (1996)).

Simulation of 195 K CO_2 isotherm and 298 K high pressure (40 bar) does not show significant no differences in adsorption sites. Figure S35 compares the probability distributions of the CO_2 molecules resulting from GCMC simulations at the two conditions.

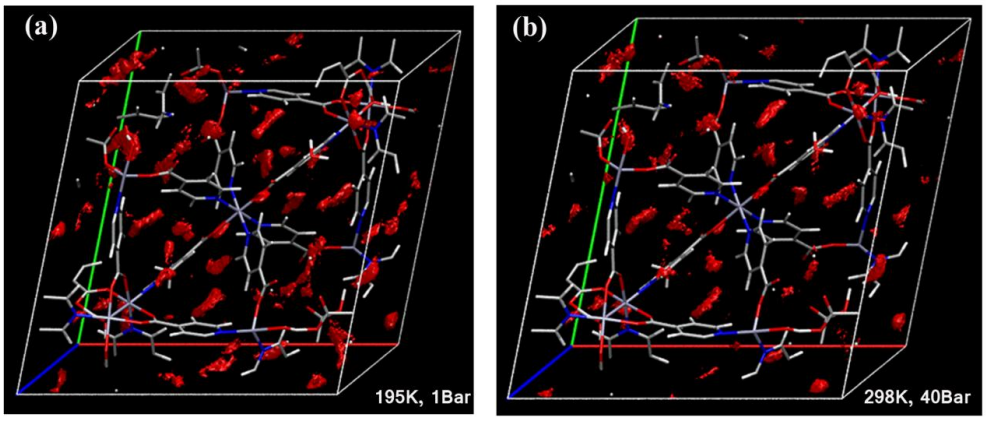

Figure S35. Probability densities of CO_2 center of mass as determined via GCMC calculations at a) 195 K and 1 bar and b) 298 K and 40 bar. The isosurface representation has an isovalue of 0.04 molecules/Å^3. The densities are very similar between low temperature, low pressure, and high temperature, high pressure.

The selectivity of CO_2 over H_2 was calculated from a binary GCMC simulation where both guest molecules were present within the GCMC simulation at the same time. This was done by specifying the partial pressures of each gas molecule with a ratio of 40:60 and 20:80 (CO_2: H_2) which is an industrially relevant mixture comparable to that found in flue gas (Ref.23 of main text) and then evaluating the uptake with this mixture using the GCMC methods that were explained above. The selectivity was calculated using the following formula,

$$Selectivity_{1,2} = \frac{\frac{q_1}{P_1}}{\frac{q_2}{P_2}} \quad \text{(S7)}$$

where q_1 is the calculated uptake of CO_2, P_1 is the partial pressure of CO_2 within the binary mixture, q_2 is the uptake of H_2, and P_2 is the partial pressure of H_2 within the binary mixture.

Isosteric heat of adsorptions (HOA) were calculated from the GCMC simulations via the Green – Kubo fluctuation theory expression,

$$q_{isosteric} = \frac{\langle UN \rangle - \langle U \rangle \langle N \rangle}{\langle N^2 \rangle - \langle N \rangle \langle N \rangle} + RT \quad \text{(S8)}$$

where N is the number of CO_2 gas molecules in the GCMC simulation and U is the total configuration energy for the CO_2 molecules (T. Vuong et al. *Langmuir* 12, 5425 (1996)). The HOA is shown to match well with experiment as shown in a previous section of this supplementary info.

12. Comparison of CO_2/H_2 selectivities of MOFs reported in the literature.

Table S11: H_2/CO_2 Selectivities from Literature

Material	Temperature (k)	Pressure (bar)	Selectivity	Composition (H_2/CO_2)	Source
Ni4PyC	313	10	229.29	60/40	This Work
		1	168.15	60/40	
		10	285.51	80/20	
		1	194.51	80/20	
CarbonJX	313	10	75	60/40	Long et al.[a]
		1	100	60/40	
		10	94	80/20	
		1	98	80/20	
Zeolite 13X	313	10	250	60/40	
		1	310	60/40	
		10	320	80/20	
		1	390	80/20	
Mg2(dobdc)	313	10	450	60/40	
		1	620	60/40	
		10	610	80/20	
		1	880	80/20	
Cu-BTTri	313	10	28	60/40	
		1	30	60/40	
		10	31	80/20	
		1	40	80/20	
MOF-177	313	10	9	60/40	
		1	9	60/40	
		10	10	80/20	
		1	10	80/20	
Co(BDP)	313	10	6	60/40	
		1	5	60/40	
		10	7	80/20	
		1	6	80/20	
Bio-MOF-11	298	10	475	10/90	Atci et al.[b] (simulated)
		1	400	10/90	
IRMOF-1	298	10	~10	10/90	Keskin et al.[c] (simulated)
		1	~10	10/90	
IRMOF-8	298	10	~10	10/90	
		1	~10	10/90	
IRMOF-10	298	10	~10	10/90	
		1	~10	10/90	

IRMOF-14	298	10	~10	10/90	
		1	~10	10/90	
COF-102	298	10	25	10/90	
		1	20	10/90	
IRMOF-9	298	10	50	10/90	
		1	90	10/90	
COF-6	298	10	75	50/50	
		1	60	50/50	
COF-8	298	10	<20	50/50	
		1	<20	50/50	
COF-10	298	10	<20	50/50	
		1	<20	50/50	
COF-102	298	10	<20	50/50	
		1	<20	50/50	
COF-103	298	10	<20	50/50	
		1	<20	50/50	
COF-105	298	10	<20	50/50	
		1	<20	50/50	Liu et al.[d] (simulated)
Cu-BTC	298	10	70	50/50	
		1	90	50/50	
IRMOF-1	298	10	<20	50/50	
		1	<20	50/50	
IRMOF-8	298	10	<20	50/50	
		1	<20	50/50	
IRMOF-10	298	10	<20	50/50	
		1	<20	50/50	
IRMOF-14	298	10	<20	50/50	
		1	<20	50/50	
IRMOF-16	298	10	<20	50/50	
		1	<20	50/50	
HKUST-1	298	1	4.52 - 6.84	50/50	Guo et al.[e]

[a]Herm, Z. R.; Swisher, J. A.; Smit, B.; Krishna, R.; Long, J. R. *J. Am. Chem. Soc.* **2011**, *133* (15), 5664. [b]Atci, E.; Erucar, I.; Keskin, S. *J. Phys. Chem. C* **2011**, *115* (14), 6833. [c]Keskin, S.; Sholl, D. S. *Langmuir* **2009**, *25* (19), 11786. [d]Liu, Y.; Liu, D.; Yang, Q.; Zhong, C.; Mi, J. *Ind. Eng. Chem. Res.* **2010**, *49* (6), 2902. [e]Guo, H.; Zhu, G.; Hewitt, I. J.; Qiu, S. *J. Am. Chem. Soc.* **2009**, *131* (5), 1646.